Importance of Strains in Kinetic Energy Flux for Submesoscale Processes from an Anisotropic Perspective

Jun Yang[1], Dongxiao Wang[1,2], Chunhua Qiu[1,2] *, Xiaoming Zhai[3], Ru Chen[4], Jiawei Qiao[5], Bo Hong[6]

[1]School of Marine Sciences, State Key Laboratory of Environmental Adaptability for Industrial Products, Sun Yat-sen University, and Southern Marine Science and Engineering Guangdong Laboratory (Zhuhai), Zhuhai, China,

[2]Guangdong Provincial Key Laboratory of Marine Resources and Coastal Engineering School of Marine Sciences, Sun Yat-sen University, Guangzhou, China,

[3]Centre for Ocean and Atmospheric Sciences, School of Environmental Sciences, University of East Anglia, Norwich, UK,

[4]Tianjin Key Laboratory for Marine Environmental Research and Service, School of Marine Science and Technology, Tianjin University, Tianjin, China,

[5]Fourth Institute of Oceanography, Ministry of Natural Resources, Beihai, China,

[6]School of Civil Engineering and Transportation, South China University of Technology, Guangzhou, China.

Corresponding author: Chunhua Qiu (qiuchh3@mail.sysu.edu.cn)

Key Points:

- A method for determining cross-scale kinetic energy flux is proposed, based on the principal axis directions of strains and eddy tilt.
- Shear strain dominates the inverse horizontal kinetic energy flux.
- The dominant factors for cross-filament symmetric and centrifugal instabilities are shear strain and anisotropic eddy kinetic energy.

Abstract

Submesoscale fronts and filaments are jet-like motions, associated with cross-scale kinetic energy (KE) flux through eddy-mean flow interaction. However, the diagnostic method for KE flux in jets with a steady zonal flow axis is not suitable for submesoscale processes with arbitrary axes. Based on a high-resolution ocean model and observations, we propose a method for diagnosing KE flux via mesoscale strains and submesoscale stresses from an anisotropic perspective. Furthermore, we develop a three-dimensional anisotropic KE flux algorithm under the hydrostatic assumption, which is important for diagnosing the energy sources and distributions of submesoscale vertical instabilities. Horizontally, we find that the inverse KE cascade mainly arises from shear strain throughout the filament's lifespan, triggering anisotropic frontogenesis and ageostrophic secondary circulations (ASCs). In ASCs, the cross-filament shear strain provides an energy source for the geostrophic shear production (GSP) and causes the forward flux through the symmetric instability. Meanwhile, the forward KE flux caused by the centrifugal instability can reach 35% of GSP which is regulated by the anisotropic eddy KE but has been neglected in previous studies. This finding effectively explains the directional dependence of strains, stresses, and instabilities, broadening our understanding of energy balance and providing a foundation for improving submesoscale parameterizations.

Plain Language Summary

Multi-scale oceanic motions, including large-scale flows (> 300 km), mesoscale eddies (50-300 km), and submesoscale processes (< 10 km), influence water matter and energy transport. The cross-scale kinetic energy (KE) exchange in larger-scale (i.e. large-scale and mesoscale) motions could be quantified by classical diagnostic methods. However, the cross-scale KE exchange for smaller-scale (i.e. submesoscale) motions remain unclear, since they usually have arbitrary flow axes and are associated with strong vertical velocities. Here, we develop an approach to diagnose cross-scale KE exchange for smaller-scale motions from an anisotropic perspective, and extend the previous 2D cross-scale KE formulation to 3D. This method could better diagnose KE sources and explain the strong vertical mechanisms for smaller-scale motions. Our findings show that, horizontally, the negative cross-scale KE exchange mainly comes from shear strain, which induces sharpening of smaller-scale motions and generates strong vertical velocities. The positive cross-scale KE exchange dominated by anisotropic stress can reach 35% of that dominated by strain. This finding is significant for understanding the development and

dynamic mechanisms of smaller-scale processes and should be incorporated into numerical models in future.

1 Introduction

The interaction between mean flow and perturbation/eddy provides an effective pathway for kinetic energy (KE) flux (Aiki & Richards, 2008; Ferrari & Wunsch, 2009; McWilliams, 2016). The cross-scale KE flux is a fundamental knowledge in oceanography, and their quantification influences the accuracy in both physical and biochemical oceanography (Gaube et al., 2014; Mahadevan, 2016; Zhang et al., 2019).

The classical method is based on the energy flux (e.g., eddy kinetic energy (EKE); mean kinetic energy (MKE), etc.) in the Lorenz energy cycle (also known as the four-box model), to quantify the reservoir, source, and sink of energy, and determine the direction of energy flux (Böning & Budich, 1992; Kang & Curchitser, 2015; Srinivasan et al., 2017; Xie et al., 2007). However, this method can only provide the global state of KE flux, and cannot capture the contribution of mean flow and eddy (Brum et al., 2023; Chu et al., 2014; Xue & Bane, 1997). For example, in KE flux, it is difficult to reflect the directional dependence of mean flow strains and eddies, limitinig discussion of the internal mechanism of KE flux. Another morphological method decomposes the eddy stress tensor and characterizes eddy stresses as ellipses (Hoskins et al., 1983; Senior et al., 2024; Stewart et al., 2015; Tamarin et al., 2016; Waterman & Lilly, 2015). By analyzing the mean flow strains along the steady direction and the tilt of the eddy ellipse, barotropic instability can be judged, and the KE flux direction can be determined (Pedlosky, 1987; Chen et al., 2024; Zeng, 1982). These morphological characteristics of the eddy ellipse can be described by its anisotropy, which includes the tilt angle, shape, and size of the ellipse (Marshall et al., 2012; Senior et al., 2024; Waterman & Hoskins, 2013). This framework based on eddy ellipses is widely used for diagnosing and analyzing KE flux under the assumption of quasi-geostrophic balance in jets in western boundary current extension regions such as the Gulf Stream and Kuroshio Extension (Marshall et al., 2012; Scott et al., 2008; Waterman et al., 2011; Waterman & Jayne, 2011). For these special jets in the western boundary current extensions, whose zonal velocity is several orders of magnitude higher than meridional velocity, only the horizontal zonal velocity strain is typically considered in previous studies.

In contrast, submesoscale filaments and fronts have the Rossby number $|R_o| \approx 1$ (where $R_o = \zeta/f$, with f as the planetary vorticity and $\zeta = \partial v/\partial x - \partial u/\partial y$ as the relative vorticity) (Capet et al., 2008; McWilliams, 2016; Qiu et al., 2023). These filaments and fronts are jet-like structures with anisotropic characteristics (Barkan et al., 2019; Mahadevan, 2016; Srinivasan et al., 2023), but their flow axes are arbitrary and mean flow strains arise from both zonal and meridional velocity. Moreover, these strong horizontal mesoscale strains can induce submesoscale frontogenesis, disrupting geostrophic balance and triggering ageostrophic secondary circulations (ASCs) with strong vertical shear KE flux (Buckingham et al., 2021; Mahadevan, 2016; McWilliams, 2017; Yu et al., 2019a). It follows that horizontal and vertical strains accompany whole submesoscale processes and play an important role in KE flux. Therefore, energy diagnostic methods developed for jets considering only zonal strain/shear are insufficient to balance the KE budget and explain the dynamic mechanisms of submesoscale fronts/filaments.

This study proposes a method to diagnose KE flux in submesoscale fronts and filaments using eddy stresses and mean flow strains, highlighting the directional dependence of KE flux on strains, stresses, and instabilities. Furthermore, we develop an anisotropic KE flux algorithm under the hydrostatic assumption and apply it to cross-filament KE flux. The organization of this paper is as follows. Section 2 presents the data and methods, Section 3 analyzes horizontal and vertical KE flux mechanisms, and Section 4 provides discussion and conclusions.

2 Data and Methods

2.1 Observations and model data

The chlorophyll-a concentration, sea surface temperature (SST), and sea level anomaly (SLA) data are derived from the Suomi National Polar-orbiting Partnership polar orbiting satellite (O'Reilly et al., 1998), the P-Tree system of the Japan Aerospace Exploration Agency (Bessho et al., 2016) and the Archiving, Validation, and Interpretation of Satellite Oceanographic project (Ducet et al., 2000), with spatial (temporal) resolutions of 750 m (daily), 2 km (hourly) and 0.25° (daily), respectively. Due to the significant impact of cloud cover on satellites, a large amount of data is missing, thus only the relatively clear SST image on 12 August, 2021 is used in this study (Figure 1c).

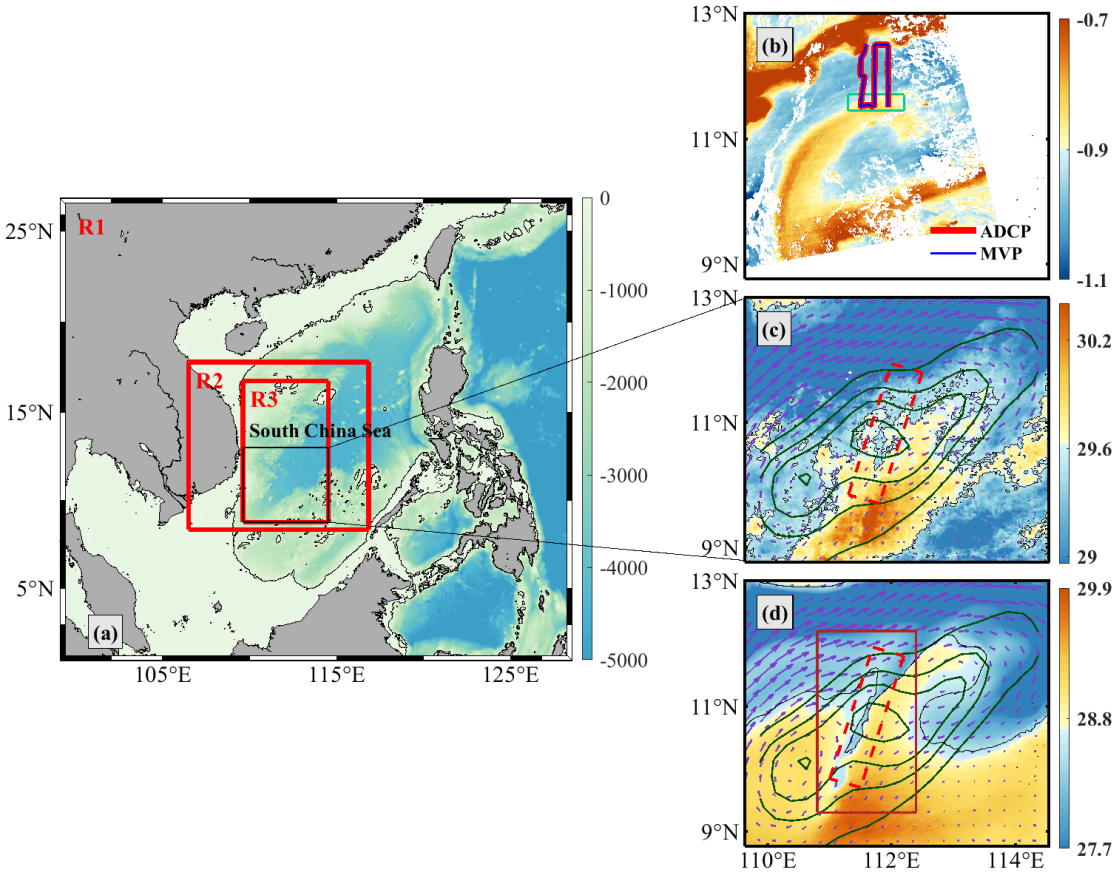

Figure 1. (a) Model nested domain and bathymetry (unit: m); (b) observation route of ADCP and MVP during 18 to 20 August, 2021 and chlorophyll-a (chla) concentration by satellites on 20 August, 2021 (unit: $\log_{10}$(chla) mg · m^{-3}); (c) observed sea surface temperature by satellite (SST) by satellite (unit: ℃); (d) simulated SST (unit: ℃). R1, R2, and R3 in (a) represent nested areas with resolutions of 21 km, 4.2 km, and 0.84 km, respectively. The black solid box is the observation area. The solid green box in (b) represents the measured data in the filament region. The time of (c) and (d) is on 12 August, 2021. The dark green contour lines represent SLA with values of 0.182 m, 0.240 m, 0.275 m, and 0.306 m from outside to inside and vector arrows represent simulated velocities in (c) and (d). The dotted red box represents the region where a filament appears in (c) and (d). The black contours in (c) and (d) are used to identify the filament position, with values of 29.55 cm and 28.5 cm, respectively. The brick-red solid box in (d) represents the main study areas below.

The in-situ profiles of temperature and salinity are collected from an AML oceanographic Moving Vessel Profiler 300 (MVP300). The profiles of current velocity, covering the upper 580 m, are obtained from a vessel-mounted 300 kHz Acoustic Doppler Current Profiler (ADCP),

which have a 2-m vertical resolution and a 5- minute temporal sampling interval. Both MVP and ADCP measurements are conducted from 18 to 20 August, 2021 (Figure 1b).

The numerical model used in this study is the Regional Ocean Modeling System (ROMS) (Cherian & Brink, 2018; Marchesiello et al., 2011; Shchepetkin & McWilliams, 2005). We set three-layer nested grids with horizontal resolutions of 21 km (R1), 4.2 km (R2), and 0.84 km (R3) (Figure 1a), respectively. Thirty-five terrain-following sigma levels are used. We interpolate the model output from sigma to Cartesian coordinates with a vertical interval of 2 m. The lateral boundary condition algorithms consist of an improved Flather-type scheme for the barotropic mode and a RadNud-type (the radiation and nudging) scheme for the baroclinic mode. The vertical subgrid mixing scheme for tracers and momentum is the Mellor-Yamada 2.5 level turbulence closure scheme. Two stretching parameters in the vertical terrain-following S coordinates are 7 and 2, controlling the bottom and surface refinements (Jing et al., 2021; Lemarié et al., 2012).

The bathymetry is derived from the Earth Topography 1 Arc-Minute Global Relief Data (ETOPO1) (Amante & Eakins, 2009). Surface forcing, including wind stress, heat flux, and freshwater flux, is generated using hourly atmospheric and oceanic reanalysis data with a $0.25° \times 0.25°$ spatial resolution from ERA5 of the European Centre for Medium-Range Weather Forecasts (ECMWF) (Soci et al., 2024), based on the linearized bulk formulation of Barnier et al. (1995).

This study focuses on a submesoscale filament, whose response time scale is about a weak. The immediacy of the process is strong, therefore, the initial oceanic state and lateral boundary information for the parent model (R1) are obtained from Hybrid Coordinate Ocean Model (HYCOM) 3-hour reanalysis dataset with a $1/12° \times 1/12°$ spatial resolution (Bleck, 2002; Chassignet et al., 2003; Halliwell, 2004). We take the daily average for HYCOM data for boundary driving the model in the R1 region. Model R1 is offline run, but the R2 and R3 are online run. The initial oceanic state and boundary of the R2 come from the output of the R1. The R2 and R3 models are created using one-way nesting from coarser to finer models (Penven et al., 2006). We adopt the hot-start mode and run the model for 31 days from 1 to 31 August, 2021 for R2 and R3 grid (Figure 1a). The model output has a temporal resolution of 3 hour.

2.2 The budget of EKE equation

The EKE equation can be used to diagnose the source and sink of KE between mesoscale and submesoscale processes (Gula & McWilliams, 2016; Kang & Curchitser, 2015; Thomas et al., 2016), as follows,

$$\underbrace{\frac{\partial \bar{k}^{xoy}}{\partial t}}_{-\mathrm{ET}} + \underbrace{\boldsymbol{\nabla}\cdot\overline{\bar{k}^{xoy}\mathbf{u}}}_{-\mathrm{TP}} + \underbrace{\frac{1}{\rho_0}\boldsymbol{\nabla}\cdot\overline{p'\mathbf{u}'}}_{-\mathrm{PW}} = \underbrace{-[\overline{u'\mathbf{u}'}\cdot\boldsymbol{\nabla}\bar{u} + \overline{v'\mathbf{u}'}\cdot\boldsymbol{\nabla}\bar{v}]}_{\Pi_{hydro}} + \underbrace{\overline{w'b'}}_{\mathrm{BF}} + \underbrace{\left(\overline{u'\mathcal{D}_u{}'} + \overline{v'\mathcal{D}_v{}'}\right) + \left(\overline{u'\mathcal{V}_u{}'} + \overline{v'\mathcal{V}_v{}'}\right)}_{\mathrm{DE}}, \tag{1}$$

where the overline denotes the mean value by a spatial filtering with a cut-off wavelength at 25 km, and the prime denotes the eddy/perturbation. $\mathbf{u}=(u, v, w)$ is the velocity vector. $b = -g\rho/\rho_0$, is the buoyancy. $\rho_0 = 1025\ \mathrm{kg}/m^3$, is the reference density. ρ is the density. $\bar{k}^{xoy} = \frac{1}{2}(\overline{u'u'} + \overline{v'v'})$, is the EKE in xoy plane. $\mathcal{V}_u$ and $\mathcal{V}_v$ are mixing terms. $\mathcal{D}_u$ and $\mathcal{D}_v$ are diffusion terms. p is the pressure. ρ_0 is the reference density. The EKE dissipation in the model is the sum of the latter two terms (Gula & McWilliams, 2016). The abbreviations of ET, TP, PW, Π_{hydro}, BF, and DE represent the KE tendency, transport production, pressure work, hydrostatic KE flux or shear production, buoyancy flux, and dissipative effect. Equation 1 is derived based on the hydrostatic assumption (see Supporting Information Equations S1, S2, S4, S5, S7, and S27 for specific derivation).

The hydrostatic KE flux, Π_{hydro}, represents the exchange of KE between the mean flow and eddy, and can be decomposed into three components:

$$\Pi_{hydro} = \underbrace{-\left[\overline{u'u'}\frac{\partial \bar{u}}{\partial x} + \overline{u'v'}\left(\frac{\partial \bar{u}}{\partial y} + \frac{\partial \bar{v}}{\partial x}\right) + \overline{v'v'}\frac{\partial \bar{v}}{\partial y}\right]}_{\Pi^{xoy}} \underbrace{-\overline{v'w'}\frac{\partial \bar{v}}{\partial z}}_{\Pi^{yoz}} \underbrace{-\overline{u'w'}\frac{\partial \bar{u}}{\partial z}}_{\Pi^{xoz}}, \tag{2}$$

where Π^{xoy}, Π^{yoz}, and Π^{xoz} are KE fluxes under the hydrostatic assumption in xoy, yoz, and xoz planes. The hydrostatic Π^{xoy} is consistent with non-hydrostatic Π^{xoy}, but Π^{yoz} and Π^{xoz} are simplified under the hydrostatic assumption. In the following text, we will present the specific derivation and simplification process.

2.3 Tensor decomposition and anisotropy definition

In the EKE equation, Π^{xoy} represents the work of Reynolds stresses against the mean flow strain (Böning & Budich, 1992; Qiu et al., 2024), and denotes the EKE production associated barotropic instability (Kang & Curchitser, 2015; Qiu et al., 2019). By introducing the

decomposition of the stress and strain tensors, we obtain isotropic and anisotropic components of stresses and strains (Hoskins et al., 1983; Qiao et al., 2023; Senior et al., 2024; Stewart et al., 2015; Waterman & Lilly, 2015) (for details, see Equation S17 in Supporting Information). By dot product of stress and strain tensors, Π^{xoy} can be decomposed into isotropic (Π_{δ}^{xoy}) and anisotropic parts (Π_{α}^{xoy}) (Qiao et al., 2023; Srinivasan et al., 2023), as follows:

$$\Pi^{xoy} = \underbrace{-\bar{k}^{xoy} \cdot \bar{\delta}^{xoy}}_{\Pi_{\delta}^{xoy}} \quad \underbrace{\underbrace{-L_n^{xoy} \cdot \bar{\alpha}_n^{xoy}}_{\Pi_{\alpha n}^{xoy}} \quad \underbrace{-L_s^{xoy} \cdot \bar{\alpha}_s^{xoy}}_{\Pi_{\alpha s}^{xoy}}}_{\Pi_{\alpha}^{xoy}}, \tag{3}$$

The Π_{α}^{xoy} can be expressed in vector form as

$$\Pi_{\alpha}^{xoy} = -|\boldsymbol{L^{xoy}}||\bar{\boldsymbol{\alpha}}^{\boldsymbol{xoy}}|\cos\left(2\theta_{\alpha}^{xoy} - 2\theta_{L}^{xoy}\right), \tag{4a}$$

where

$$\boldsymbol{L^{xoy}} = L_n^{xoy}\boldsymbol{i} + L_s^{xoy}\,\boldsymbol{j} = |\boldsymbol{L^{xoy}}|\cos 2\theta_L^{xoy}\,\boldsymbol{i} + |\boldsymbol{L^{xoy}}|\sin 2\theta_L^{xoy}\,\boldsymbol{j}, \tag{4b}$$

$$\bar{\boldsymbol{\alpha}}^{\boldsymbol{xoy}} = \bar{\alpha}_n^{xoy}\boldsymbol{i} + \bar{\alpha}_s^{xoy}\,\boldsymbol{j} = |\bar{\boldsymbol{\alpha}}^{\boldsymbol{xoy}}|\cos 2\theta_{\alpha}^{xoy}\boldsymbol{i} + |\bar{\boldsymbol{\alpha}}^{\boldsymbol{xoy}}|\sin 2\theta_{\alpha}^{xoy}\boldsymbol{j}, \tag{4c}$$

where the bold fonts represent vectors. $\boldsymbol{i}$ and $\boldsymbol{j}$ are unit vectors at x and y axes. All δ and α in the right subscripts denote the isotropic and anisotropic components of variables, respectively (except for the principal direction of the strain, such as θ_{α}^{xoy}, which denotes the most significant direction of the strain). All the s and n in the right subscripts represent the components of variables in the directions of shear and normal strain. The right superscripts xoy, yoz, and xoz represent three two-dimensional coordinate planes. $\Pi_{\alpha n}^{xoy}$ and $\Pi_{\alpha s}^{xoy}$ are anisotropic KE fluxes from normal and shear strain, respectively. $\bar{\delta}^{xoy} = \frac{\partial \bar{u}}{\partial x} + \frac{\partial \bar{v}}{\partial y}$ is the divergence of mean flow in xoy plane. $\bar{\boldsymbol{\alpha}}^{\boldsymbol{xoy}}$ is the vector of mean strains. $|\bar{\boldsymbol{\alpha}}^{\boldsymbol{xoy}}| = \sqrt{\bar{\alpha}_n^{xoy2} + \bar{\alpha}_s^{xoy2}}$ is the mean flow strain rate. $\bar{\alpha}_n^{xoy} = \frac{\partial \bar{u}}{\partial x} - \frac{\partial \bar{v}}{\partial y}$ and $\bar{\alpha}_s^{xoy} = \frac{\partial \bar{u}}{\partial y} + \frac{\partial \bar{v}}{\partial x}$ are the components of $\bar{\boldsymbol{\alpha}}^{\boldsymbol{xoy}}$, called the normal (stretch) and shear strain. $\theta_{\alpha}^{xoy} = \frac{1}{2}\arctan\left(\frac{\bar{\alpha}_s^{xoy}}{\bar{\alpha}_n^{xoy}}\right)$ is the principal axis direction of strains. $\boldsymbol{L^{xoy}}$ is the vector of excess EKE of velocity fluctuations in the major axis direction compared with the minor axis direction. $L_n^{xoy} = \frac{\overline{u'u'} - \overline{v'v'}}{2}$ and $L_s^{xoy} = \overline{u'v'}$ are the components of $\boldsymbol{L^{xoy}}$, called the

normal stress difference and the shear stress. $|\boldsymbol{L^{xoy}}| = \sqrt{L_n^{xoy\,2} + L_s^{xoy\,2}}$ is the anisotropic EKE and is a measure of the EKE associated with the anisotropic portion of the velocity fluctuations. This parameter is referred to simply as the ellipse anisotropy (Marshall et al., 2012; Senior et al., 2024; Waterman & Hoskins, 2013). $\theta_L^{xoy} = \frac{1}{2}\arctan\left(\frac{L_s^{xoy}}{L_n^{xoy}}\right)$ is the eddy tilt angle.

Based on the three-dimensional Navier-Stokes equation, we can obtain the three-dimensional non-hydrostatic KE flux (Delpech et al., 2024; Qiao et al., 2023) (see Supporting Information S1 to S9 for specific derivation), as follows:

$$\Pi_{non-hydro} = -[\overline{u'\mathbf{u}'} \cdot \boldsymbol{\nabla}\bar{u} + \overline{v'\mathbf{u}'} \cdot \boldsymbol{\nabla}\bar{v} + \overline{w'\mathbf{u}'} \cdot \boldsymbol{\nabla}\bar{w}], \tag{5}$$

Following Qiao et al. (2023), we decompose Equation 5 into isotropic, anisotropic, and compensation terms:

$$\Pi_{non-hydro} = \left(\Pi_\alpha^{xoy} + \Pi_\alpha^{yoz} + \Pi_\alpha^{xoz}\right) + \Pi_\delta^{3D} + \Pi_*, \tag{6}$$

where

$$\Pi_\alpha^{yoz} = -\left[\frac{1}{2}(\overline{v'v'} - \overline{w'w'})\left(\frac{\partial\bar{v}}{\partial \mathrm{y}} - \frac{\partial\bar{w}}{\partial \mathrm{z}}\right) + \overline{v'w'}\left(\frac{\partial\bar{v}}{\partial z} + \frac{\partial\bar{w}}{\partial \mathrm{y}}\right)\right], \tag{7}$$

$$\Pi_\alpha^{xoz} = -\left[\frac{1}{2}(\overline{u'u'} - \overline{w'w'})\left(\frac{\partial\bar{u}}{\partial \mathrm{x}} - \frac{\partial\bar{w}}{\partial \mathrm{z}}\right) + \overline{u'w'}\left(\frac{\partial\bar{u}}{\partial z} + \frac{\partial\bar{w}}{\partial \mathrm{x}}\right)\right], \tag{8}$$

$\Pi_\delta^{3D} = -\bar{k}^{3D}\boldsymbol{\nabla}\cdot\bar{\mathbf{u}}$ is the three-dimensional isotropic KE flux. $\bar{k}^{3D} = \frac{1}{2}(\overline{u'u'} + \overline{v'v'} + \overline{w'w'})$ and $\boldsymbol{\nabla}\cdot\bar{\mathbf{u}} = \frac{\partial\bar{u}}{\partial x} + \frac{\partial\bar{v}}{\partial y} + \frac{\partial\bar{w}}{\partial z}$ are the three-dimensional EKE and divergence. $\Pi_* = \frac{1}{2}\left(\overline{u'u'}\frac{\partial\bar{u}}{\partial x} + \overline{v'v'}\frac{\partial\bar{v}}{\partial y} + \overline{w'w'}\frac{\partial\bar{w}}{\partial z}\right)$ is the compensation term of three-dimensional KE flux.

Comparing the KE flux in Equations 1, 2, and 5, we find that $\Pi_{non-hydro}$ satisfies the relationship: $\Pi_{non-hydro} = \Pi_{hydro} + \overline{w'\mathbf{u}'} \cdot \boldsymbol{\nabla}\bar{w}$. Under the hydrostatic assumption, the vertical momentum equation simplifies to $g = -\frac{1}{\rho}\frac{\partial p}{\partial z}$, implying that the advection term satisfies $\mathbf{u} \cdot \boldsymbol{\nabla}w = 0$. Consequently, the three-dimensional KE flux satisfies $\overline{w'\mathbf{u}'} \cdot \boldsymbol{\nabla}\bar{w} \approx 0$. Therefore, there is $\Pi_{hydro} \approx \Pi_{non-hydro} - 0$, that is, Π_{hydro} is the KE flux under the hydrostatic assumption. Hydrostatic and non-hydrostatic Π_α^{xoy} are consistent, but Π_α^{yoz} and Π_α^{xoz} in Equations 7 and 8 can be written as:

$$\Pi_{\alpha}^{yoz} = -\left(\frac{1}{2}\overline{v'v'}\frac{\partial \bar{v}}{\partial y} + \overline{v'w'}\frac{\partial \bar{v}}{\partial z}\right) \tag{9}$$

$$\Pi_{\alpha}^{xoz} = -\left(\frac{1}{2}\overline{u'u'}\frac{\partial \bar{u}}{\partial x} + \overline{u'w'}\frac{\partial \bar{u}}{\partial z}\right) \tag{10}$$

For clarity, we use the superscript "c" to denote the xoy, yoz, and xoz coordinate planes. Considering that the submesoscale process still satisfies hydrostatic balance, the three-dimensional KE flux of non- hydrostatic pressure by Qiao et al. (2023) may overestimate the vertical KE flux (Equation 7, and 8) (Haine & Marshall, 1998; Mahadevan, 2006; Thomas et al., 2016).

The anisotropic KE fluxes within these planes can be expressed in vector form as:

$$\Pi_{\alpha}^{c} = \underbrace{-L_n^c \cdot \bar{\alpha}_n^c}_{\Pi_{\alpha n}^c} \underbrace{-L_s^c \cdot \bar{\alpha}_s^c}_{\Pi_{\alpha s}^c} = -|\boldsymbol{L}^c||\bar{\boldsymbol{\alpha}}^c|\cos(2\theta_{\alpha}^c - 2\theta_L^c) \tag{11}$$

The meaning of $\bar{\boldsymbol{\alpha}}^{\boldsymbol{c}}$ and $\boldsymbol{L}^{\boldsymbol{c}}$, and their components and principal axis directions are consistent with the same variables mentioned above in the xoy plane, but the coordinates are different. Note that under the hydrostatic assumption, the components of $\bar{\boldsymbol{\alpha}}^{\boldsymbol{c}}$ and $\boldsymbol{L}^{\boldsymbol{c}}$ in the yoz and xoz planes, are simplified compared to the same variables in the xoy plane. For example, there are $\bar{\alpha}_n^{yoz} = \frac{\partial \bar{v}}{\partial y}$, $\bar{\alpha}_s^{yoz} = \frac{\partial \bar{v}}{\partial z}$, $\bar{\alpha}_n^{xoz} = \frac{\partial \bar{u}}{\partial x}$, $\bar{\alpha}_s^{xoz} = \frac{\partial \bar{u}}{\partial z}$, $L_n^{yoz} = \frac{1}{2}\overline{v'v'}$ $L_s^{yoz} = \overline{v'w'}$, $L_n^{xoz} = \frac{1}{2}\overline{u'u'}$, and $L_s^{xoz} = \overline{u'w'}$.

In general, Π_{α}^{yoz} and Π_{α}^{xoz} are used to describe the vertical anisotropic KE flux along and across fronts/filaments. In this article, the general direction of the filament flow axes is determined by R_o. Considering that normal and shear strains may vary with the coordinate system, it is meaningful to discuss those components in a fixed coordinate system. To facilitate the study of cross-filament KE flux, we rotate the horizontal coordinate axis clockwise so that the flow axis aligns with the meridional direction parallel (see Supporting Information Figure S1). Similarly, for the observed filament, we rotate coordinate axis by 90° counterclockwise to discuss its Π_{α}^{xoz}. In the cross-filament region, the horizontal mean flow is primarily geostrophic, indicating that the submesoscale process adheres to the quasi-geostrophic balance (Shearman et al., 1999; Thomas et al., 2008; Chai & Zhao, 2024). Therefore, the horizontal velocity is replaced by the geostrophic velocity (u_g, v_g) in Π_{α}^{yoz} and Π_{α}^{xoz}.

2.4 Quasi-geostrophic omega equation

To illustrate the in-situ KE budget, the quasi -geostrophic omega equation, which is more appropriate for submesoscale dynamics, is utilized to calculate vertical velocity based on observations (Hu et al., 2011; Martin & Richards, 2001; Molemaker et al., 2010; Pietri et al., 2021), as follows:

$$f^2 \frac{\partial^2 w}{\partial z^2} + N^2 \left(\frac{\partial^2}{\partial x^2} + \frac{\partial^2}{\partial y^2} \right) w = \nabla_h \cdot \boldsymbol{Q}, \tag{12a}$$

where

$$\boldsymbol{Q} = \left[2f \left(\frac{\partial v_g}{\partial x} \frac{\partial u_g}{\partial z} + \frac{\partial v_g}{\partial y} \frac{\partial v_g}{\partial z} \right), -2f \left(\frac{\partial u_g}{\partial x} \frac{\partial u_g}{\partial z} + \frac{\partial u_g}{\partial y} \frac{\partial v_g}{\partial z} \right) \right], \tag{12b}$$

is the so-called Q-vector (Hoskins, 1982). $N^2 = \frac{\partial b}{\partial z}$ is the square of buoyancy frequency. For a detailed analysis of the validity of the quasi-geostrophic omega equation at submesoscales, please refer to Pietri et al. (2021).

3 Results

3.1 Characteristics of submesoscale filaments

Submesoscale filaments and fronts often occur at the edges of mesoscale eddies (Callies et al., 2016; Klein & Lapeyre, 2009; McWilliams, 2016). In the western South China Sea in summer, coupled mesoscale eddies often appear on both sides of the offshore eastward jet in southeastern Vietnam (Fang et al., 2002; Li et al., 2014). The SLA map and the simulated flow field capture two anticyclonic eddies in south of this offshore eastward jet on 12 August, 2021 (Figures 1c and 1d). Both of the SST from satellite observations and numerical simulations show a cold tongue extending to warm water in the core of the right eddy (the red dashed box in Figures 1c and 1d), which is the characteristic of a cold filament. Another significant submesoscale filament is captured by in-situ observations over the western South China Sea (Figure 1b). Note that the position and time of modelled filament are different from that of the observed filament (Figures 1b and 1c), and we choose the part of observation in the edge of that filament (the green box in Figure 1b).

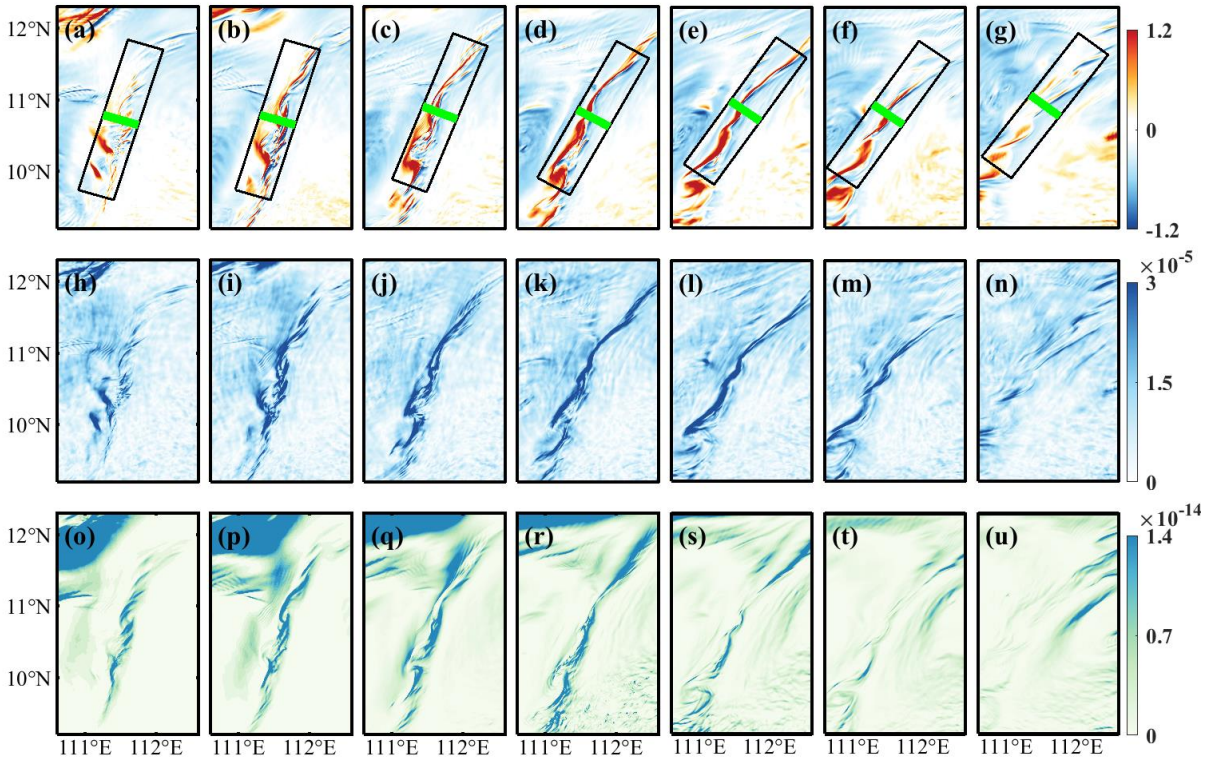

Figure 2. (a) ~ (g), (h) ~ (n), and (o) ~ (u) are daily simulated surface Rossby number (R_o), surface flow strain rate ($|\alpha^{xoy}| = \sqrt{\left(\frac{\partial u}{\partial x} - \frac{\partial v}{\partial y}\right)^2 + \left(\frac{\partial v}{\partial x} + \frac{\partial u}{\partial y}\right)^2}$, unit: s^{-1}), and frontal sharpness ($|\nabla_h b|^2$, unit: s^{-4}) from 9 to 15 August, 2021. The black boxes are the filament area selected based on R_o and the light green line represents the cross-filament region. The area of this figure is the brick-red box in Figure 1d.

To determine the flow axis and the dynamic evolution of the filament, we define the lifespan of the filament based on the area of $|R_o| \approx 1$ and $|\alpha| > 2 \times 10^{-5}\ s^{-1}$. The lifespan is approximately 7 days from formation to dissipation during 9 to 15 August, 2021(Figures 2a to 2g), which is divided into four stages: generation (slow increase on 9 August), development (rapid increase during 10 and 11 August), maturity (relatively stable on 12 August), and extinction (slow decrease during 13 to15 August).

There is a sharp increase of $|R_o| \approx 1$ area from 10 to 12 August, indicating that submesoscale motion is most active at that period. The strong strain is associated with the whole filament lifespan (Figures 2h to 2n), which means that there is a strong horizontal shear and stretch process. The strong strain is conducive to the increase of horizontal buoyancy gradient,

thus enhancing frontogenesis sharpness (Figures 2o to 2u), which indicates that the strong frontogenesis may be one of important reasons for the formation and enhancement of the filament (McWilliams et al., 2009; Gula & McWilliams, 2014; Wang et al., 2022).

3.2 KE balance at the filament

To distinguish motions between mesoscale and submesoscale, the KE spectrum is used to determine the spatial filtering scale (Figure 3a). Following previous studies, submesoscale motions are identified where the KE spectrum slope approaches k^{-2} (Cheng et al., 2023; Qiu et al., 2023; Qiu et al., 2024). In the nested region R3, the KE spectrum exhibits a slope approximately parallel to k^{-2} at scales smaller than 25 km (Figure 3a). Therefore, 25 km is selected as the cutoff wavelength for high-pass filtering, with signals below this threshold defined as submesoscale processes. To remove the signals of near-inertial internal waves and other high-frequency variabilities, we apply a daily average to the 3-hourly output data (Cheng et al., 2023; Zhang et al., 2019; Zhang et al., 2023).

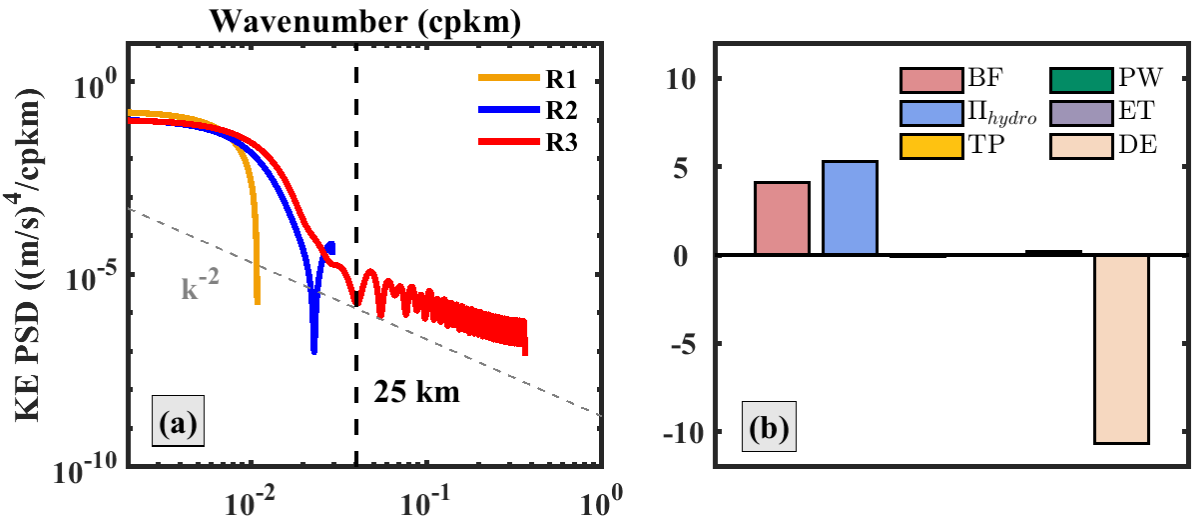

Figure 3. (a) Kinetic energy power spectrum; (b) vertical and regional average of EKE equation terms (unit: 1×10^{-11} W kg^{-1}) for the filament region (black dashed box in Figure 1c). In (a), R1 (yellow), R2 (blue), and R3 (red) refer to the nested models, respectively; the black dashed line represents the cut-off wavelength of 25 km, and grey dashed line is the reference slope k^{-2}. The abbreviations of ET, TP, PW, Π_{hydro}, BF, and DE represent KE tendency, transport production, pressure work, hydrostatic KE flux, buoyancy flux, and dissipative effect in (b).

The EKE equation is often adopted to diagnose the energy budget in eddy-current interactions (Evans et al.,2022; Haine & Marshall, 1998; Thomas & Taylor, 2013). The diagnostic results indicate that the main source of KE is Π_{hydro} (Figure 3b). The vertical mean Π_{hydro} is positive and accounts for 55% of the entire KE source (Figure 3b), indicating a strong interaction between mesoscale mean flow and submesoscale perturbation in the filament.

3.3 KE flux at the filament

The active KE within a fixed ocean domain is stored as MKE and EKE, which convert between each other through barotropic instability driven by Reynolds stresses (Greatbatch et al., 2010; Kang & Curchitser, 2015; Zha & Marshall, 2013). When $\Pi^{xoy} > 0$, the barotropic instability occurs, indicating that KE is transferred from larger scale MKE to smaller scale EKE (Böning and Budich, 1992; Chu et al., 2014; Qiu et al., 2019), representing a forward KE cascade; conversely, a negative value indicates an inverse cascade. That is:

$$\Pi^{xoy} \begin{cases} < 0, & \text{EKE} \rightarrow \text{MKE} \\ = 0, & \text{neutral} \\ > 0, & \text{MKE} \rightarrow \text{EKE} \end{cases} \tag{13}$$

Following Equation 3, Π^{xoy} consists of isotropic and anisotropic parts (Π_{δ}^{xoy} and Π_{α}^{xoy}). The vertical mean Π_{δ}^{xoy} exhibits a strong forward KE cascade over the entire filament lifespan, while Π_{α}^{xoy} is always negative, driving an inverse KE cascade (Figure 4a). We compare the directional similarity rate (SR, that is, points whose Π_{α}^{xoy} and Π^{xoy} have the same the positive or negative direction) in the filament region. SR exceeds 76% in entire filament lifespan, and the maximum can reach 91%. This means that Π_{α}^{xoy} dominates the direction of KE flux in this region (Figure 4a).

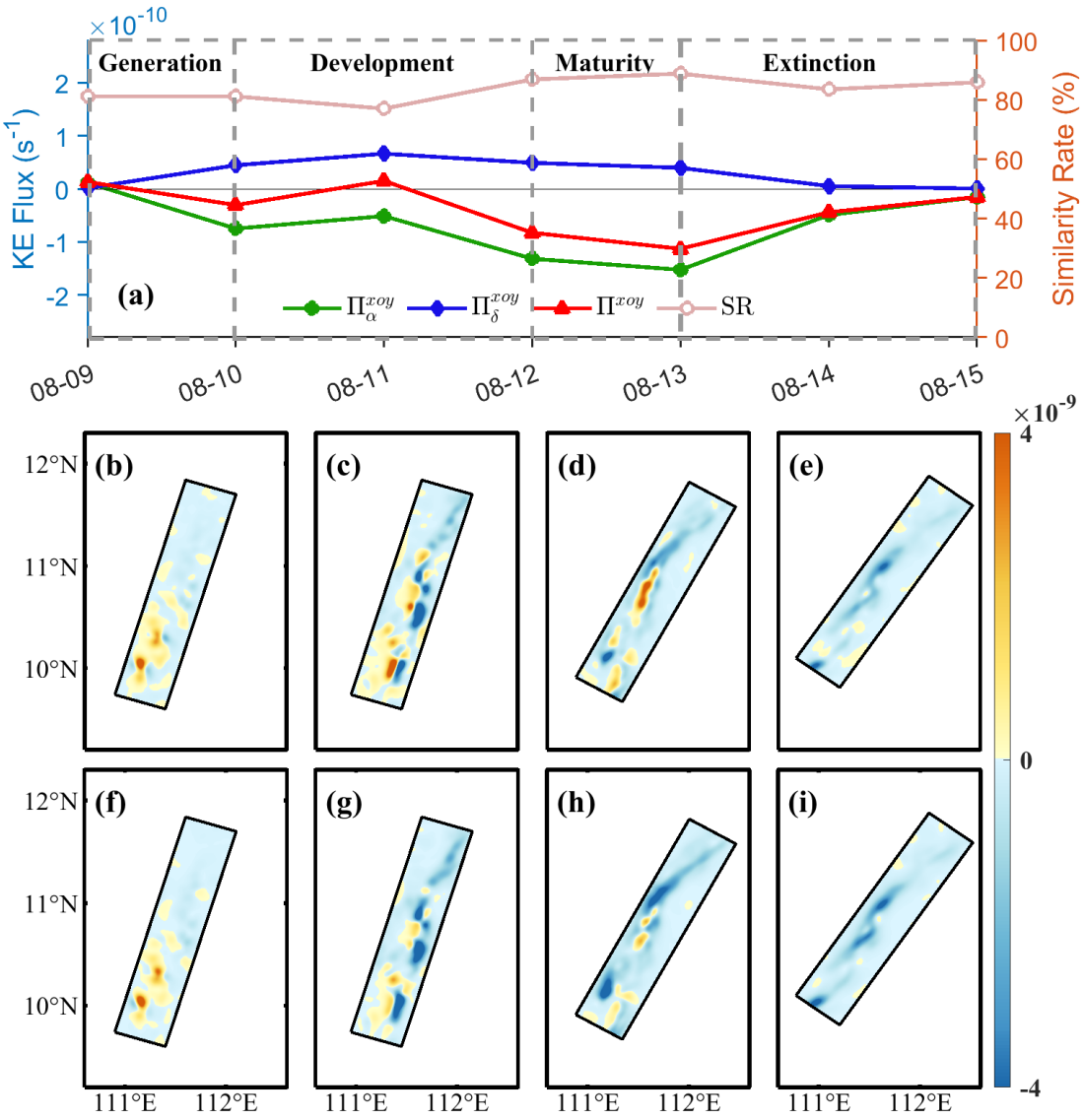

Figure 4. (a) Vertical spatial mean of kinetic energy flux (Π^{xoy}), isotropic kinetic energy flux (Π_{δ}^{xoy}), anisotropic kinetic energy flux (Π_{α}^{xoy}), and similarity rate of Π^{xoy} and Π_{α}^{xoy} in the mixed layer. (b) ~ (e) and (f) ~ (i) are vertical mean of Π^{xoy} and Π_{α}^{xoy} in generation, development, maturity, and extinction stages.

The spatial distributions of forward cascades from Π_{α}^{xoy} and Π^{xoy} are almost the same (Figures 4b to 4i), while negative KE cascades are mainly contributed by Π_{α}^{xoy}. This indicates that Π_{α}^{xoy} predominantly governs the direction of KE flux, whereas Π_{δ}^{xoy} has minimal spatial influence. This result agrees with previous studies. Srinivasan et al. (2023) analyzed the energy flux through a Helmholtz decomposition and showed that anisotropic KE flux chiefly drives the

inverse cascade, while both isotropic and anisotropic productions contribute to the forward cascade. Qiao et al. (2023) found that isotropic production has little impact on KE flux direction when considering large-scale to mesoscale processes.

It can be concluded that Π_{α}^{xoy} dominates the direction of Π^{xoy}. Therefore, we propose a new criterion for identifying KE flux direction by neglecting Π_{δ}^{xoy},

$$\Pi^{xoy} = -|\boldsymbol{L^{xoy}}||\bar{\boldsymbol{\alpha}}^{\boldsymbol{xoy}}|\cos\left(\theta_{\alpha}^{xoy} - \theta_{L}^{xoy}\right)\begin{cases} < 0, & \text{EKE} \rightarrow \text{MKE} \\ = 0, & \text{neutral} \\ > 0, & \text{MKE} \rightarrow \text{EKE} \end{cases} \tag{14}$$

Since $|\boldsymbol{L^{xoy}}|$ and $|\bar{\boldsymbol{\alpha}}^{\boldsymbol{xoy}}|$ are positive values, the key factor controlling the KE flux direction is the absolute angle difference $\left|\theta_{\alpha}^{xoy} - \theta_{L}^{xoy}\right|$:

$$\left|\theta_{\alpha}^{xoy} - \theta_{L}^{xoy}\right|\begin{cases} < 45°, & \text{EKE} \rightarrow \text{MKE} \\ = 45°, & \text{neutral} \\ > 45°, & \text{MKE} \rightarrow \text{EKE} \end{cases} \tag{15}$$

Equation 15 shows that the bidirectional KE flux between different scales is determined by the eddy tilt and the principal axis direction of the mean flow strains, explaining the instantaneous stresses and strains state as well as the critical angle for KE conversion direction.

If Equation 15 is extended to the three-dimensional planes, we have

$$|\theta_{\alpha}^{c} - \theta_{L}^{c}|\begin{cases} < 45°, & \text{EKE} \rightarrow \text{MKE} \\ = 45°, & \text{neutral} \\ > 45°, & \text{MKE} \rightarrow \text{EKE} \end{cases} \tag{16}$$

The previous morphological diagrams of KE flux determined by shear and normal strains and eddy variance ellipse are shown in Figures 5a and 5b (Pedlosky, 1987; Chen et al., 2024; Zeng, 1982), in which only the horizontal zonal velocity strain is considered and not suitable for submesoscale filaments and fronts with arbitrary flow axes. The relationship among EKE, MKE, eddy tilt, and the principal axis direction of mean flow strains based on Equation 16 is shown in Figure 5c. When $|\theta_{\alpha}^{c} - \theta_{L}^{c}| > 45°$, KE is transfered from the mean flow to eddy/perturbation (MKE→EKE), indicating a forward KE cascade. On the contrary, $|\theta_{\alpha}^{c} - \theta_{L}^{c}| < 45°$ indicates an inverse KE cascade from the eddy to the mean flow (EKE → MKE). This method comprehensively accounts for all strains and stresses in KE flux, enabling quantification of their directional contributions.

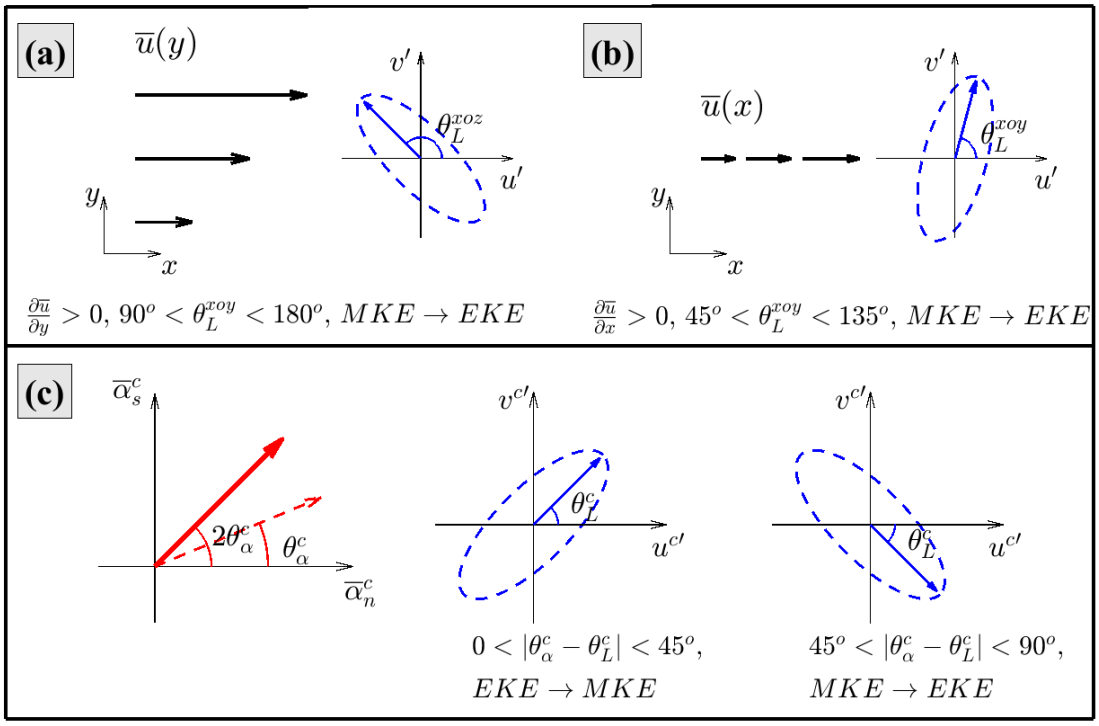

Figure 5. (a) and (b) are two diagrams of kinetic energy flux by shear and normal strains and eddy variance ellipse at $v = 0$, respectively. (c) is a diagram of three-dimensional KE flux by the strain rate vector and the eddy variance ellipse, which is drawn based on Equations 13 and 16. (u^c, v^c) are (u, v), (v, w), and (u, w) in xoy, yoz, and xoz planes.

3.3.1 Horizontal KE flux at the filament

Submesoscale filaments are stretched and compressed in along- and cross-filament directions by mesoscale strains, resulting in elongated filaments and active energy interactions (Lin et al., 2020; Mahadevan, 2006; Zhang et al., 2019). The horizontal KE flux is strongest during the mature stage (Figures 4a and 7a), and thus we select the average value from this stage to investigate the KE mechanism. Within the filament, both $|\boldsymbol{L}^{\boldsymbol{xoy}}|$ and $|\overline{\boldsymbol{\alpha}}^{\boldsymbol{xoy}}|$ are strong, indicating significant anisotropy and strain (Figures 6a and 6e), which provides favorable conditions for Π_α^{xoy} to drive the cross-scale KE flux (Figure 6h). In the directional view, $2\theta_\alpha^{xoy}$ approaches 90°, indicating that the strain rate is predominantly governed by shear strain. θ_L^{xoy} determines the magnitude of $\left|\theta_\alpha^{xoy} - \theta_L^{xoy}\right|$, and thus controls the direction of the KE flux (Figures 6b to 6d, and 6h).

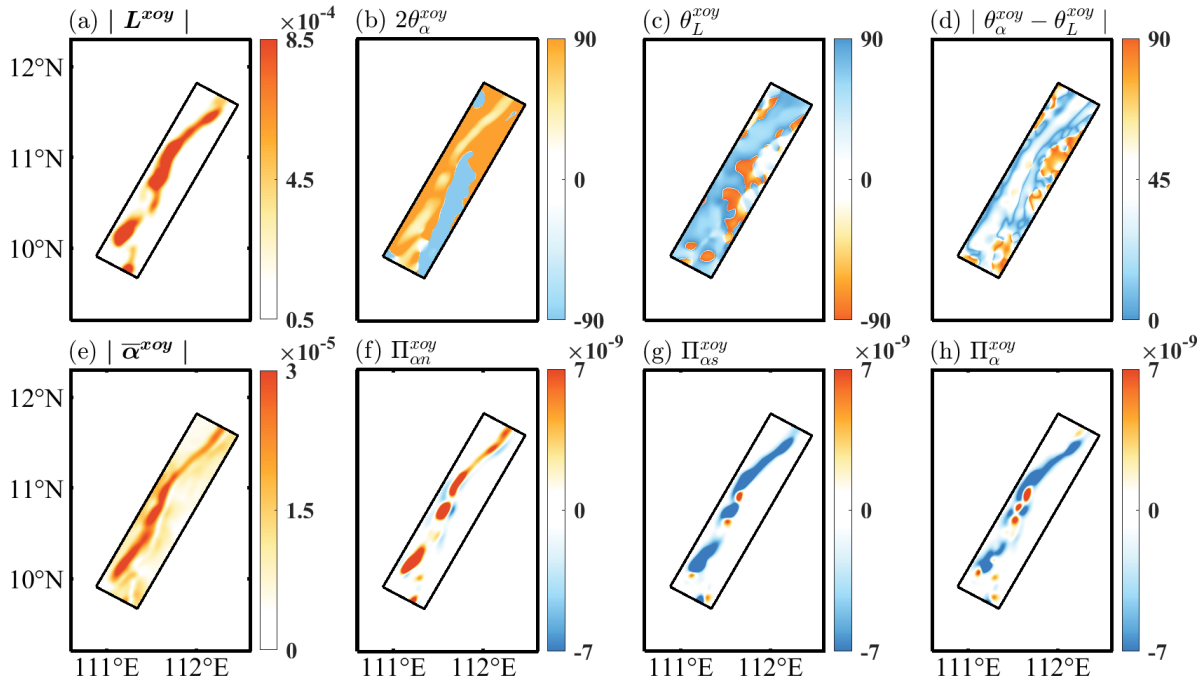

Figure 6. (a) Anisotropic eddy kinetic energy, $|\boldsymbol{L^{xoy}}|$ (unit: $m^2 \cdot s^{-1}$); (b) double principal axis direction of strains, $2\theta_{\alpha}^{xoy}$ (unit: °); (c) eddy tilt angle, θ_{L}^{xoy} (unit: °); (d) absolute value of angle difference between θ_{α}^{xoy} and θ_{L}^{xoy} (unit: °); (e) strain rate of mean flow, $|\overline{\boldsymbol{\alpha}^{xoy}}|$ (unit: s^{-1}); (f) anisotropic normal kinetic energy flux, $\Pi_{\alpha n}^{xoy}$ (unit: s^{-1}); (g) anisotropic shear kinetic energy flux, $\Pi_{\alpha s}^{xoy}$ (unit: s^{-1}); (h) anisotropic horizontal kinetic energy flux, Π_{α}^{xoy} (unit: s^{-1}). (a) ~ (h) are vertical mean values in the maturity stage in the mixed layer.

From the contribution of strains, $\Pi_{\alpha s}^{xoy}$ is the main source of the inverse Π_{α}^{xoy} (Figures 6g and 6h). In Π_{α}^{xoy}, there are $\theta_{L}^{xoy} \to 90°$ and $2\theta_{\alpha}^{xoy} \to 90°$ (Figures 6b and 6c), that is, $\bar{\alpha}_{s}^{xoy} \gg \bar{\alpha}_{n}^{xoy}$ and $L_{s}^{xoy} \ll L_{n}^{xoy}$ (refer to Equations 4a, 4b, and 4c), indicating the inverse cascades of $\Pi_{\alpha s}^{xoy} = -L_{s}^{xoy} \cdot \bar{\alpha}_{s}^{xoy}$ are dominated by shear strain $\bar{\alpha}_{s}^{xoy}$. Combined with the relationship among $\Pi_{\alpha s}^{xoy}$, Π_{α}^{xoy} and Π^{xoy}, it is evident that the shear strain, $\bar{\alpha}_{s}^{xoy}$, is the primary contributor to the horizontal inverse KE cascade (Figures 4a and 7a). In contrast, $\Pi_{\alpha n}^{xoy}$ is primarily influenced by the normal stress difference, and exhibits a weaker forward cascade during the mature stage, contributing little to the total anisotropic KE flux, Π_{α}^{xoy} (Figures 6f and 6h).

To verify the applicability of the above conclusion, we used the daily (5 to 12 January, 2012) LLC4320 (from Massachusetts Institute of Technology general circulation model (MITgcm) on a latitude-longitude-polar cap (LLC) grid) data in the Kuroshio Extension, with a

horizontal resolution of $1/48°$, to calculate the horizontal anisotropic KE flux and its components (Qiu et al., 2018; Yu et al., 2019b; Zhang et al., 2023). We obtained the same conclusion as above conclusion that the shear strain is the main contributor for the inverse KE fluxes (Figure S3 in Supporting Information), confirming that our method is applicable to eddy-rich regions with strong currents.

3.3.2 Strain-induced frontogenesis associated with the evolution of the filament

When a horizontal strain acts on a lateral buoyancy gradient (Figures 2h to 2u), strain-induced frontogenesis occurs (Mahadevan, 2006; McKie et al., 2024; McWilliams et al., 2015; Zhang et al., 2019). Submesoscale fronts and filaments are identified as the flow with anisotropic buoyancy gradients and velocity gradients (Barkan et al., 2019; Srinivasan et al., 2023). If the horizontal buoyancy gradient tensor $\boldsymbol{B} = \begin{bmatrix} b_x^2 & b_x b_y \\ b_x b_y & b_y^2 \end{bmatrix}$ is introduced into the frontal tendency (F) (Srinivasan et al., 2023), which is used to characterize frontogenesis ($F > 0$) and frontolysis ($F < 0$) processes, we can divide the frontal tendency into isotropic (F_δ) and anisotropic parts (F_α),

$$F = \underbrace{-\frac{\left(b_x^2 + b_y^2\right)}{2} \cdot \delta^{xoy}}_{F_\delta} \quad \underbrace{-\frac{\left(b_x^2 - b_y^2\right)}{2} \cdot \alpha_n^{xoy} - b_x b_y \cdot \alpha_s^{xoy}}_{F_\alpha} \tag{17a}$$

$$= \underbrace{-\frac{1}{2}|\nabla_h b|^2 \cdot \delta^{xoy}}_{F_\delta} \quad \underbrace{\underbrace{-\frac{\left(b_x^2 - b_y^2\right)}{2} \cdot \alpha_n^{xoy}}_{F_{\alpha n}} \quad \underbrace{-b_x b_y \cdot \alpha_s^{xoy}}_{F_{\alpha s}}}_{F_\alpha} \tag{17b}$$

where $b_x = \frac{\partial b}{\partial x}$ and $b_y = \frac{\partial b}{\partial y}$ are horizontal buoyancy gradients. $F_{\alpha n}$ and $F_{\alpha s}$ represent the anisotropic normal and shear frontal tendency, respectively. $|\nabla_h b|^2 = b_x^2 + b_y^2$, is frontal sharpness. Equation 17 presents a method to decompose frontal tendency into strain directions, facilitating the quantification of strain contributions to frontogenesis and frontolysis processes. Frontogenesis is a key mechanism in the development and sharpening of fronts (Gula & McWilliams, 2016; McWilliams et al., 2009; Buckingham et al., 2021). It induces upwelling and surface divergence on the lighter side of a front, and downwelling and surface convergence on the denser side, generating a strong vertical velocity that drives an ASC (Jing et al., 2021; Siegelman, 2020; Thomas et al., 2008). Similar to the previous text, we transform the meridional

coordinates to coincide with the principal flow axis of the filament so that the relative contributions of divergence and strain and its components on frontogenesis can be explicitly separated (Balwada et al., 2021; Hetland et al., 2025; Srinivasan et al., 2023). We find that F_{α} dominates the frontogenesis, reaching its maximum during the development stage of the filament, while F_{δ} contributes only slightly (Figure 7b). For the contribution of strain components, anisotropic shear frontogenesis $F_{\alpha s}$ is the primary driver of filament sharpening (Figure 7b). This indicates that frontogenesis is mainly concentrated along the shear direction, promoting ASCs (Figures 8c and 8g) and triggering vertical instabilities. Recently, Hetland et al. (2025) proposed a "strain efficiency" concept unambiguously defined the contribution of total strain. This method may provide us with inspiration for completely decomposing the frontogenesis although it did not discuss the contribution of buoyancy gradient.

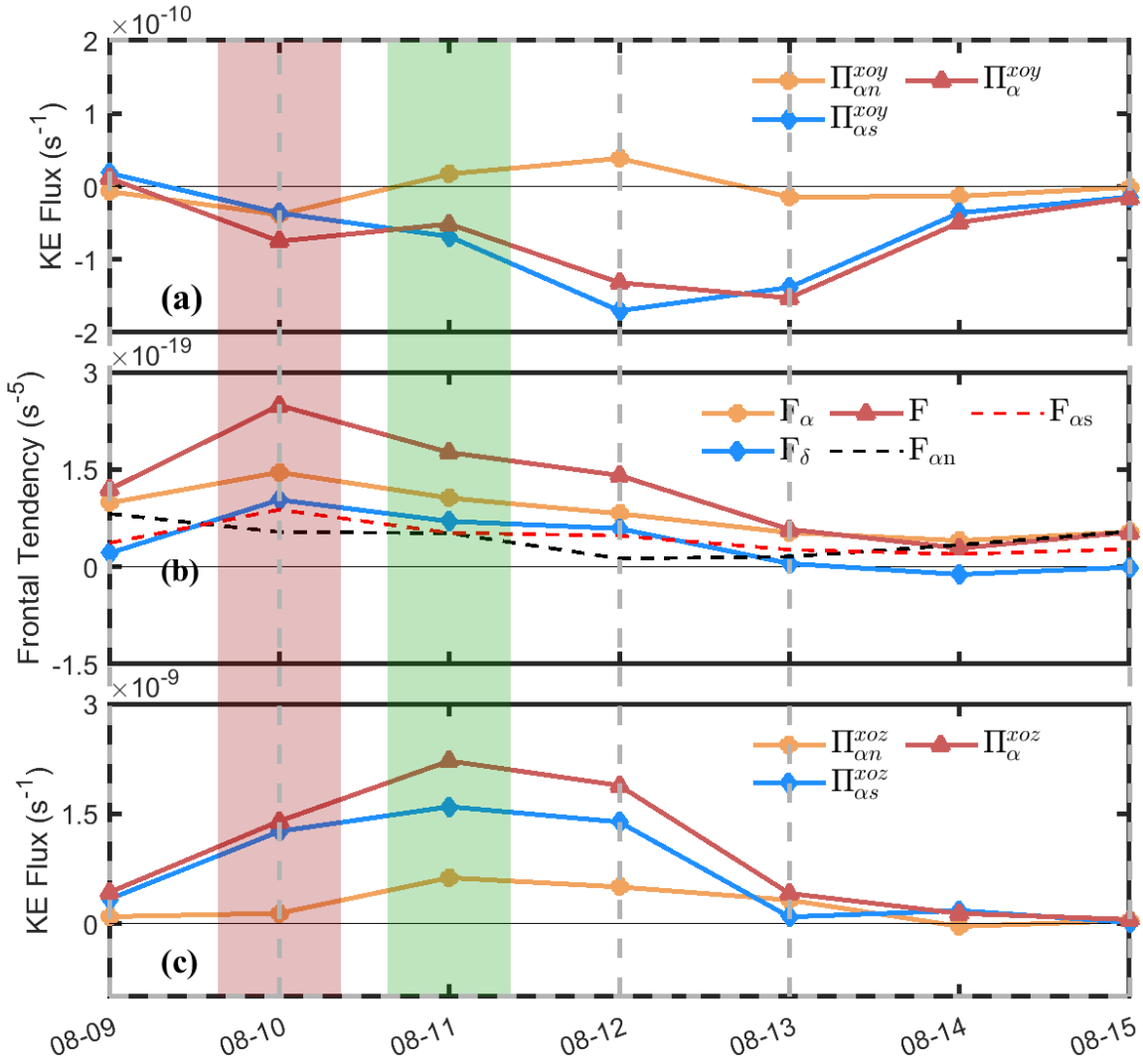

Figure 7. (a) Horizontal anisotropic energy flux (unit: s^{-1}); (b) frontal tendency (unit: s^{-5}); (c) cross-filament anisotropic energy flux (unit: s^{-1}). The variables from (a) to (c) are the average values in the mixed layer from 9 to 15 August, 2021. The gray dashed box represents the four stages of the filament (generation, development, maturity, and extinction). The two grey boxes are the two typical KE flux points on 10 August (the first point (P1)) and 11 August (the second point (P2)), respectively.

3.3.3 Vertical KE flux and associated submescale instabilities in ASCs

The ASCs induced by frontogenesis intensify the vertical exchange in the mixed layer, and may trigger cross-filament submesoscale vertical instabilities, promoting KE dissipation to smaller scales (McWilliams et al., 2004; Srinivasan et al., 2023). The cross-filament KE flux

435 mainly exhibits a forward cascade, with two typical time points throughout the filament lifespan
436 (Figure 7c). The first point occurs at the beginning of development stage (10 August), and is
437 overwhelmingly dominated by $\Pi_{\alpha s}^{xoz}$. The second point appears during the development stage (11
438 August), resulting from the combined action of $\Pi_{\alpha s}^{xoz}$ and $\Pi_{\alpha n}^{xoz}$. Both of them show a forward KE
439 cascade, markedly different from the horizontal KE flux. This suggests distinct mechanisms
440 operate at these two stages. We will focus on studying the cross-filament KE mechanism at these
441 points.

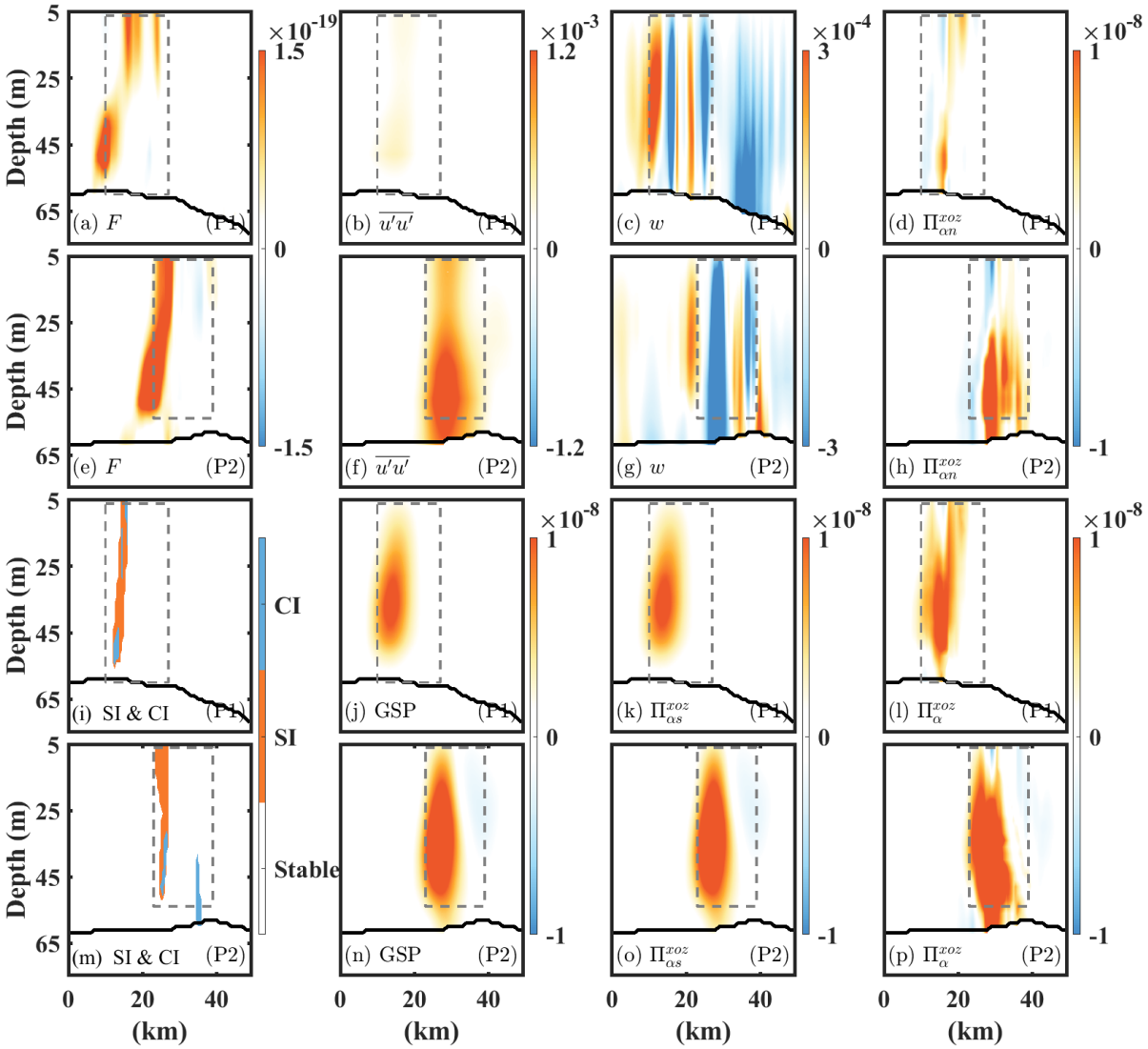

442

443 **Figure 8**. (a) frontal tendency, F (unit: s^{-5}); (b) zonal eddy stress, $\overline{u'u'}$ (unit: $m^2 \cdot s^{-2}$); (c) vertical flow velocity, w
444 (unit: $m \cdot s^{-1}$); (d) anisotropic normal kinetic energy flux, $\Pi_{\alpha n}^{xoz}$(unit: s^{-1}); (i) instabilities; (j) geostrophic shear
445 production (GSP) (unit: s^{-1}); (k) anisotropic shear kinetic energy flux, $\Pi_{\alpha s}^{xoz}$ (unit: s^{-1}); (l) simulated anisotropic

446 kinetic energy flux, Π_{α}^{xoz} (unit: s^{-1}). (a) ~ (d) and (i) ~ (l) are the variables on 10 August (the first point (P2)). The
447 variables of (e) ~ (h) and (m) ~ (p) are variables on 11 August (the second point (P2)).

448

449 Once fronts and filaments form and intensify, they may become susceptible to a variety of
450 instabilities that generate additional submesoscale currents (Gula & McWilliams, 2014; Jing et
451 al., 2021; Thomas & Taylor, 2010). In particular, when the horizontal buoyancy gradient and
452 vertical stratification vary sharply in geostrophic flow, negative Ertel potential vorticity (that is,
453 $fq < 0$, where $fq = f(f + \zeta)N^2 - |\nabla_h b|^2$ and $N^2 = \frac{\partial \mathrm{b}}{\partial z}$) may occur, resulting in symmetric
454 instability (SI) (Dong et al., 2022; Haine & Marshall, 1998; Thomas et al., 2016) (Figures 8i and
455 8m) (see Figure S2 in the Supporting Information for instabilities diagnose). SI extracts energy
456 from the geostrophic shear production (GSP, where $\mathrm{GSP} = -\overline{u'w'}\frac{\partial \overline{u_g}}{\partial z}$), which characterizes the
457 conversion rate of KE obtained from geostrophic flow with only vertical shear, and transfers it to
458 smaller scales for dissipation (Bachman et al., 2017; Taylor & Thompson, 2023; Thomas et al.,
459 2013) (Figures 8e and 8m). Comparing GSP with Equation 10 reveals that $\Pi_{\alpha s}^{xoz}$ is consistent
460 with GSP under the hydrostatic assumption, that is, $\mathrm{GSP} \approx \Pi_{\alpha s}^{xoz}$, indicating that the cross-
461 filament GSP is distributed in the shear direction. Rose diagram of the cross-filament strain and
462 anisotropic EKE at the two points are shown in Figure 9. At the first point, there are $2\theta_{\alpha}^{xoz} \approx$
463 $\pm 90°$ and $\theta_L^{xoz} \approx -90°$ (Figures 9a and 9c), indicating that $\overline{\boldsymbol{\alpha}}^{xoz}$ is mainly concentrated in the
464 shear direction while L_n^{xoz} is mainly concentrated in the normal direction. This suggests that the
465 energy driving SI mainly comes from the cross-filament geostrophic shear strain at the first point,
466 consistent with previous studies (Dong et al., 2022; McWilliams, 2016; Qiu et al., 2024).

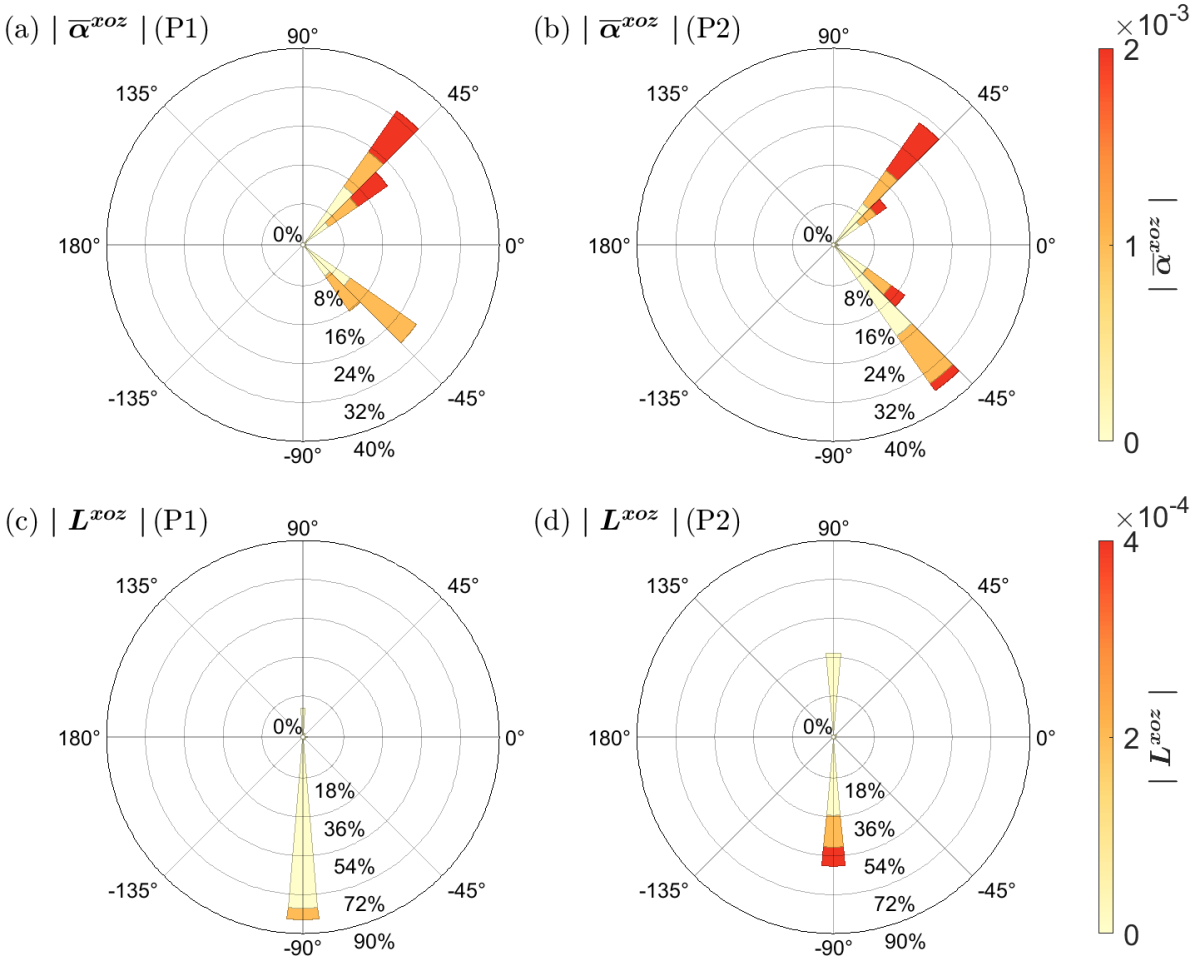

Figure 9. (a) and (b) are the rose graphs of strain rate of mean flow, $\bar{\alpha}^{xoz}$ (unit: s^{-1}), and (c) and (d) are the rose graphs of anisotropic eddy kinetic energy, $\boldsymbol{L}^{xoz}$ (unit: $m^2 \cdot s^{-1}$) at the first point (P1) and second point (P2).

At the second point, the contributions of $\Pi_{\alpha n}^{xoz}$ can reach 35% of $\Pi_{\alpha s}^{xoz}$, which means that there may be another path of forward flux besides SI. The distribution of θ_{α}^{xoz} and θ_{L}^{xoz} at the second point is consistent with those at the first point (Figures 9b and 9d), which means that $\Pi_{\alpha s}^{xoz}$ and $\Pi_{\alpha n}^{xoz}$ are dominated by the shear strain α_s^{xoz} and the normal stress difference L_n^{xoz}, respectively. The difference is that $\overline{\boldsymbol{\alpha}}^{xoz}$ at the second point decreases and $\boldsymbol{L}^{xoz}$ increases overall (Figures 9b and 9d), which means that $\Pi_{\alpha s}^{xoz}$ is weakened and $\Pi_{\alpha n}^{xoz}$ is enhanced (Figures 8h and 8o). Under the hydrostatic assumption, there is $L_n^{xoz} = \frac{\overline{u'u'}}{2}$ (Equation 10), which means that the stress $\overline{u'u'}$ dominant the forward cascade of $\Pi_{\alpha n}^{xoz}$. In the filament, the increase of $\overline{u'u'}$ is typically driven by the extraction of KE from the laterally shear geostrophic current through

centrifugal/inertial instability (CI/II) (Figures 8i and 8m). The onset of CI requires that $f(f + \zeta_g) < 0$ and $N^2 > 0$ (Gula & McWilliams, 2016; Thomas et al., 2013) (see Figure S2 in the Supporting Information for instabilities diagnose). Therefore, the forward cascade caused by CI can reach 35% of GSP caused by SI at the second point (Figures 7c and 8h, 8m and 8n), which is one of the key mechanisms responsible for the rapid intensification of cross-filament KE flux over a short timescale.

To verify the direction dependence of the submesoscale vertical instabilities and their associated KE flux, we derive Π_{α}^{xoz} based on observational data. The vertical velocity is estimated using the quasi-geostrophic omega equation (Equation 12a). We focus on the strongest ASC zone near the filament edge and compute the associated KE flux (Figures 1b and 10a). The results suggest that the anisotropic normal production driven by CI accounts for approximately 29% of the GSP (Figures 10c and 10d), almost consistent with the model outcomes (35%). This means that the KE flux caused by vertical instabilities exhibits significant direction dependence, and the contributions of strain and anisotropic EKE are significantly different in different directions. This contrasts with previous studies, which often focused solely on the overall strength and trend of KE flux while overlooking the underlying mechanisms involving internal stresses and strains (Brannigan et al., 2017; Jing et al., 2021; Thomas et al., 2016; Yu et al., 2019b). Note that we investigate vertical KE fluxes and instability mechanisms in both cross- and along-filament directions through coordinate transformation. Recent studies, such as Chen et al. (2024) and Hetland et al. (2025), have proposed frameworks for decomposing KE fluxes and frontogenesis in filament-aligned coordinates, which provide valuable references for future work.

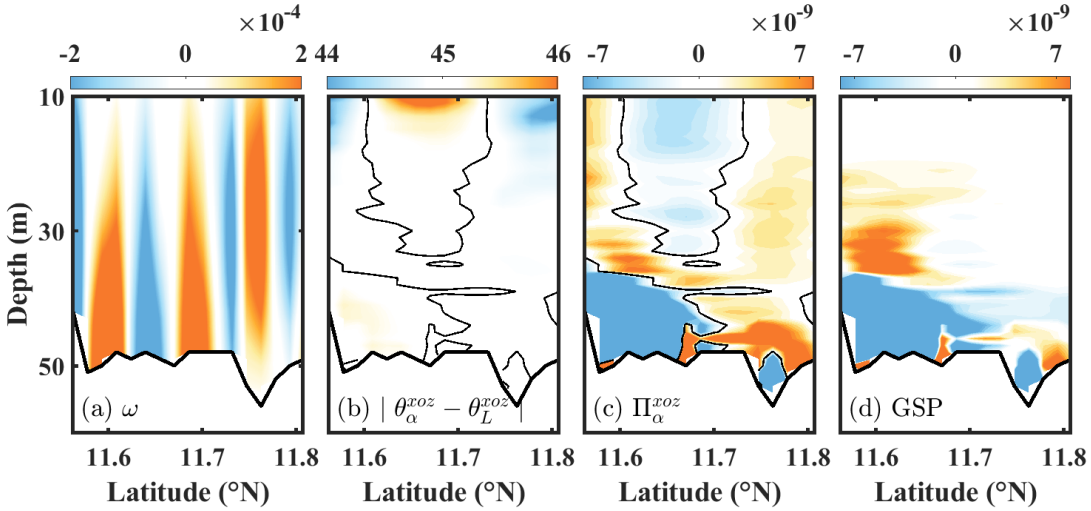

Figure 10. (a) Omega vertical flow velocity, ω (unit: m/s); (b) absolute angle difference between θ_{α}^{xoz} and θ_{L}^{xoz} (unit: °); (b) anisotropic kinetic energy flux, Π_{α}^{xoz} (mod) (unit: s^{-1}); (d) geostrophic shear production, GSP (unit: s^{-1}). Variables in (a) ~ (d) are calculated based on observations.

Although the KE flux and frontogenesis of the filament are mainly concentrated within the mixed layer, there is also KE flux penetrating below the mixed layer (Figure 8p). Recently, Zhang et al. (2021) proposed the concept of mixed transitional layer instability, suggesting that baroclinic instability in these layers ultimately generates deep-penetrating and surface-intensified submesoscales (Zhang, 2024). This implies that the current study may underestimate baroclinic frontogenesis and instabilities occurring below the mixed layer—an aspect worth quantifying in future work.

4 Summary and Discussion

Based on a high-resolution ROMS model and observations, we propose a novel method for identifying three-dimensional KE flux using mesoscale strains and submesoscale eddy stresses from an anisotropic perspective. According to the state of the Rossby number and strain rate, we divide the filament evolution into four stages: generation, development, maturity and extinction. We found that the direction of KE flux within the filament is primarily governed by eddy tilt. Horizontally, the inverse KE cascade throughout the entire lifespan is mainly driven by shear strain. This strong shear strain promotes the formation of strain-induced frontogenesis with pronounced anisotropy. Anisotropic shear frontogenesis is the primary mechanism for filament

522 sharpening, which disrupts the geostrophic balance and generates ASCs across the filament.
523 Within ASCs, we find that the GSP originates from the Π_{as}^{xoz}, indicating that KE is transferred
524 from mesoscale to dissipative scales by SI mainly due to shear strain. Π_{an}^{xoz} provides a forward
525 KE flux driven by CI and modulated by the normal stress difference. Π_{an}^{xoz} can reach up to 35%
526 of GSP, playing a key role in regulating the generation, development, and decay of ASCs—an
527 aspect that has been largely overlooked in previous studies.

528 Based on the hydrostatic assumption, our method improves the anisotropic three-
529 dimensional non-hydrostatic KE flux from Qiao et al. (2023), and is used to diagnose the
530 contributions of strain and stress in the cross- and along-filament/front KE conversion, as well as
531 their responses to instabilities. This method extends the KE diagnosis to eddy-mean flow
532 interactions from large-mesoscale jets to submesoscale filaments and fronts with arbitrary axes,
533 highlighting the strong strain characteristics of submesoscale processes. In addition, for the
534 decomposition of strain-induced frontogenesis, this paper emphasizes the direction dependence
535 of the horizontal buoyancy gradient and strains, offering a new perspective for parameterizing
536 submesoscale instabilities (Bachman et al., 2017; Naveira Garabato et al., 2022; Zhang et al.,
537 2023). At broader scales, our method remains applicable to KE exchanges between large-scale
538 and mesoscale flows, as well as between mesoscale eddies and near-inertial waves, and similar
539 methods have been confirmed in other studies (Delpech et al., 2024; Guo et al., 2024; Polzin,
540 2010; Qiao et al., 2023).

541 This article emphasizes the role of mesoscale strain and anisotropic EKE in energy flux.
542 Therefore, the origin of frontogenesis is considered within the traditional framework, in which
543 the balanced strain field is the primary driver of the frontogenesis (Hoskins & Bretherton 1972;
544 Lapeyre & Klein 2006; McWilliams et al., 2009). However, the vertical momentum mixing
545 under the turbulent thermal wind (TTW) balance can also alter the horizontal density gradient of
546 fronts, potentially influencing the evolution of submesoscale frontogenesis (Barkan et al., 2019;
547 Gula et al., 2014; Sullivan & McWilliams, 2024; Wenegrat et al., 2020; Wenegrat et al., 2023).
548 Using the Large Eddy Simulation, Sullivan & McWilliams (2018) and Pham & Sarkar (2019)
549 found that ASCs suppresses vertical buoyancy flux via surface turbulence. More recently,
550 Johnson & Fox Kemper (2024) has demonstrated that this suppression is not captured by
551 traditional boundary layer turbulence theory. If TTW acts as a source of potential vorticity within
552 the mixed layer, it may suppress SI in submesoscale fronts (McWilliams et al., 2016; Wenegrat

et al., 2018; Barkan et al., 2019). This implies that our estimates of cross-filament frontogenesis and SI based solely on GSP may be overestimated.

In addition, this paper focuses on KE flux and strain-induced frontogenesis intensification, while overlooking the available potential energy generated by the mixed layer instability (MLI) (Boccaletti et al., 2007; Callies et al., 2016; Cao et al., 2022; Capet et al., 2008). Recent work by Schubert et al. (2020) has shown that submesoscale eddies driven by MLI can gradually evolve into sharp fronts and trigger ASCs, leading to forward KE flux. Therefore, investigating the impact of vertical turbulent mixing and MLI on strain fields and KE flux will be an important focus of future research.

Acknowledgments

This study was supported by the National Key R&D Program of China (Grant 2023YFC3107801), and National Natural Science Foundation of China (Nos. 42376011, 42227901). We thank for the technical support of the National Large Scientific and Technological Infrastructure "Earth System Numerical Simulation Facility" (https://cstr.cn/31134.02.EL).

Conflict of Interest Statement

The authors have no conflicts of interest to disclose.

Data Availability Statement

The sea level anomaly from AVISO satellite altimeter is available at https://data.marine.copernicus.eu/product/SEALEVEL_GLO_PHY_L4_MY_008_047/services from Ducet et al. (2000).The ETOPO1 data is freely available at https://www.ngdc.noaa.gov/mgg/global/relief/ETOPO1/data/ice_surface/grid_registered/binary/ from Amante and Eakins (2009). The HYCOM data is available at https://ncss.hycom.org/thredds/catalogs/GLBy0.08/expt_93.0.html from Bleck (2002), Chassignet et al. (2003), and Halliwell (2004). The ERA5 data is available at https://rda.ucar.edu/datasets/d633000/ from Soci et al. (2024). The ocean model ROMS 4.1 is obtained from the ROMS website (https://github.com/myroms/roms/tree/develop/ROMS). The sea level anomaly from Ducet et al. (2000), the SST from Bessho et al. (2016), the model inputs, and the plot data for reproducing the results of this work are available from Yang et al. (2025). All data were processed using MATLAB Mathworks (2022).

Reference

Aiki, H., & Richards, K. J. (2008). Energetics of the Global Ocean: The Role of Layer-Thickness Form Drag. *Journal of Physical Oceanography*, *38*(9), 1845–1869. https://doi.org/10.1175/2008JPO3820.1

584 Amante, C., & Eakins, B. W. (2009). ETOPO1 1 Arc-Minute Global Relief Model: Procedures,
585 data sources and analysis [Dataset]. National Geophysical Data Center, NOAA.
586 https://doi.org/10.7289/V5C8276M
587 Aluie, H., Hecht, M., & Vallis, G. K. (2018). Mapping the Energy Cascade in the North Atlantic
588 Ocean: The Coarse-Graining Approach. *Journal of Physical Oceanography*, *48*(2), 225–
589 244. https://doi.org/10.1175/JPO-D-17-0100.1
590 Bachman, S. D., Fox-Kemper, B., Taylor, J. R., & Thomas, L. N. (2017). Parameterization of
591 Frontal Symmetric Instabilities. I: Theory for Resolved Fronts. *Ocean Modelling*, *109*, 72–
592 95. https://doi.org/10.1016/j.ocemod.2016.12.003
593 Balwada, D., Xiao, Q., Smith, S., Abernathey, R., & Gray, A. R. (2021). Vertical fluxes
594 conditioned on vorticity and strain reveal submesoscale ventilation. *Journal of Physical*
595 *Oceanography*, *51*(9), 2883-2901. https://doi.org/10.1175/JPO-D-21-0016.1
596 Barkan, R., Molemaker, M. J., Srinivasan, K., McWilliams, J. C., & D'Asaro, E. A. (2019). The
597 Role of Horizontal Divergence in Submesoscale Frontogenesis. *Journal of Physical*
598 *Oceanography*, *49*(6), 1593–1618. https://doi.org/10.1175/JPO-D-18-0162.1
599 Barnier, B., Siefridt, L., & Marchesiello, P. (1995). Thermal forcing for a global ocean
600 circulation model using a three-year climatology of ECMWF analyses. *Journal of Marine*
601 *Systems*, *6*(4), 363–380. https://doi.org/10.1016/0924-7963(94)00034-9
602 Bessho, K., Date, K., Hayashi, M., Ikeda, A., Imai, T., Inoue, H., et al. (2016). An Introduction
603 to Himawari-8/9—Japan's New-Generation Geostationary Meteorological Satellites.
604 *Journal of the Meteorological Society of Japan. Ser. II*, *94*(2), 151–183.
605 https://doi.org/10.2151/jmsj.2016-009

606 Bleck, R. (2002). An oceanic general circulation model framed in hybrid isopycnic-cartesian
607 coordinates. *Ocean Modelling*, *4*(1), 55–88. https://doi.org/10.1016/S1463-5003(01)00012-
608 9
609 Boccaletti, G., Ferrari, R., & Fox-Kemper, B. (2007). Mixed Layer Instabilities and
610 Restratification. *Journal of Physical Oceanography*, *37*(9), 2228–2250.
611 https://doi.org/10.1175/JPO3101.1
612 Böning, C. W., and R. G. Budich (1992), Eddy dynamics in a primitive equation model:
613 Sensitivity to horizontal resolution and friction. *Journal of Physical Oceanography*, *22*(4),
614 361–381. https://doi.org/10.1175/1520-0485(1992)022<0361:EDIAPE>2.0.CO;2
615 Brannigan, L., Marshall, D. P., Naveira Garabato, A. C., Nurser, A. J. G., & Kaiser, J. (2017).
616 Submesoscale Instabilities in Mesoscale Eddies. *Journal of Physical Oceanography*,
617 *47*(12), 3061–3085. https://doi.org/10.1175/JPO-D-16-0178.1
618 Brum, A. L., Azevedo, J. L. L. de, & Dengler, M. (2023). Energetics of eddy–mean flow
619 interactions in the deep western boundary current off the northeastern coast of Brazil. *Deep*
620 *Sea Research Part I: Oceanographic Research Papers*, *193*, 103965.
621 https://doi.org/10.1016/j.dsr.2023.103965
622 Buckingham, C. E., Gula, J., & Carton, X. (2021). The Role of Curvature in Modifying Frontal
623 Instabilities. Part I: Review of Theory and Presentation of a Nondimensional Instability
624 Criterion. *Journal of Physical Oceanography*, *51*(2), 299–315. https://doi.org/10.1175/JPO-
625 D-19-0265.1
626 Callies, J., Flierl, G., Ferrari, R., & Fox-Kemper, B. (2016). The role of mixed-layer instabilities
627 in submesoscale turbulence. *Journal of Fluid Mechanics*, *788*, 5–41.
628 https://doi.org/10.1017/jfm.2015.700

629 Cao, H., & Jing, Z. (2022). Submesoscale Ageostrophic Motions Within and Below the Mixed
630 Layer of the Northwestern Pacific Ocean. *Journal of Geophysical Research: Oceans*,
631 *127*(2), e2021JC017812. https://doi.org/10.1029/2021JC017812
632 Capet, X., McWilliams, J. C., Molemaker, M. J., & Shchepetkin, A. F. (2008). Mesoscale to
633 Submesoscale Transition in the California Current System. Part I: Flow Structure, Eddy
634 Flux, and Observational Tests. *Journal of Physical Oceanography*, *38*(1), 29–43.
635 https://doi.org/10.1175/2007JPO3671.1
636 Chai, J., & Zhao, J. (2024). Characteristics of the Kinetic Energy Spectra in the Subpolar North
637 Atlantic. *Journal of Physical Oceanography*, *54*(1), 29–44. https://doi.org/10.1175/JPO-D-
638 22-0247.1
639 Chassignet, E. P., Smith, L. T., Halliwell, G. R., & Bleck, R. (2003). North Atlantic Simulations
640 with the Hybrid Coordinate Ocean Model (HYCOM): Impact of the Vertical Coordinate
641 Choice, Reference Pressure, and Thermobaricity. *Journal of Physical Oceanography*,
642 *33*(12), 2504–2526. https://doi.org/10.1175/1520-
643 0485(2003)033<2504:NASWTH>2.0.CO;2
644 Chen, R., Yang, Y., Geng, Q., Stewart, A., Flierl, G., & Wang, J. (2024). Diagnostic Framework
645 Linking Eddy Flux Ellipse with Eddy-Mean Energy Exchange. *Ocean-Land-Atmosphere*
646 *Research*, *3*, 0072. https://doi.org/10.34133/olar.0072
647 Cheng, X., Li, L., Jing, Z., Cao, H., Zhou, G., Duan, W., & Zhou, Y. (2023). Seasonal Features
648 and Potential Mechanisms of Submesoscale Processes in the Southern Bay of Bengal during
649 2011/12. *Journal of Physical Oceanography*, *53*(4), 1199–1217.
650 https://doi.org/10.1175/JPO-D-22-0078.1

Cherian, D. A., & Brink, K. H. (2018). Shelf Flows Forced by Deep-Ocean Anticyclonic Eddies at the Shelf Break. *Journal of Physical Oceanography*, *48*(5), 1117–1138. https://doi.org/10.1175/JPO-D-17-0237.1

Chu, X., Xue, H., Qi, Y., Chen, G., Mao, Q., Wang, D., & Chai, F. (2014). An exceptional anticyclonic eddy in the South China Sea in 2010. *Journal of Geophysical Research: Oceans*, *119*(2), 881–897. https://doi.org/10.1002/2013JC009314

Delpech, A., Barkan, R., Srinivasan, K., McWilliams, J. C., Arbic, B. K., Siyanbola, O. Q., & Buijsman, M. C. (2024). Eddy–Internal Wave Interactions and Their Contribution to Cross-Scale Energy Fluxes: A Case Study in the California Current. *Journal of Physical Oceanography*, *54*(3), 741–754. https://doi.org/10.1175/JPO-D-23-0181.1

Dong, J., Fox‐Kemper, B., Jing, Z., Yang, Q., Tian, J., & Dong, C. (2022). Turbulent Dissipation in the Surface Mixed Layer of an Anticyclonic Mesoscale Eddy in the South China Sea. *Geophysical Research Letters*, *49*(16), e2022GL100016. https://doi.org/10.1029/2022GL100016

Ducet, N., Le Traon, P. Y., & Reverdin, G. (2000). Global high‐resolution mapping of ocean circulation from TOPEX/Poseidon and ERS‐1 and ‐2. *Journal of Geophysical Research: Oceans*, *105*(C8), 19477–19498. https://doi.org/10.1029/2000JC900063

Evans, D. G., Frajka-Williams, E., & Naveira Garabato, A. C. (2022). Dissipation of mesoscale eddies at a western boundary via a direct energy cascade. *Scientific Reports*, *12*(1), 887. https://doi.org/10.1038/s41598-022-05002-7

Fang, W., Fang, G., Shi, P., Huang, Q., & Xie, Q. (2002). Seasonal structures of upper layer circulation in the southern South China Sea from in situ observations. *Journal of Geophysical Research: Oceans*, *107*(C11). https://doi.org/10.1029/2002JC001343

Ferrari, R., & Wunsch, C. (2009). Ocean Circulation Kinetic Energy: Reservoirs, Sources, and Sinks. *Annual Review of Fluid Mechanics*, *41*(1), 253–282. https://doi.org/10.1146/annurev.fluid.40.111406.102139

Gaube, P., McGillicuddy, D. J., Chelton, D. B., Behrenfeld, M. J., & Strutton, P. G. (2014). Regional variations in the influence of mesoscale eddies on near‐surface chlorophyll. *Journal of Geophysical Research: Oceans*, *119*(12), 8195–8220. https://doi.org/10.1002/2014JC010111

Greatbatch, R. J., Zhai, X., Claus, M., Czeschel, L., & Rath, W. (2010). Transport driven by eddy momentum fluxes in the Gulf Stream Extension region. *Geophysical Research Letters*, *37*(24), 2010GL045473. https://doi.org/10.1029/2010GL045473

Gula, J., Molemaker, M. J., & McWilliams, J. C. (2014). Submesoscale Cold Filaments in the Gulf Stream. *Journal of Physical Oceanography*, *44*(10), 2617–2643. https://doi.org/10.1175/JPO-D-14-0029.1

Gula, J., Molemaker, M. J., & McWilliams, J. C. (2016). Topographic generation of submesoscale centrifugal instability and energy dissipation. *Nature Communications*, *7*(1), 12811. https://doi.org/10.1038/ncomms12811

Guo, X., Yang, X.-Y., Deng, Q., Lin, H., & Wang, D. (2024). Rhythms of the Agulhas current within the framework of energetic anisotropy. *Journal of Geophysical Research*: *Oceans*, *129*, e2024JC021044. https://doi.org/10.1029/2024JC021044

Haine, T. W. N., & Marshall, J. (1998). Gravitational, Symmetric, and Baroclinic Instability of the Ocean Mixed Layer. *Journal of Physical Oceanography*, *28*(4), 634–658. https://doi.org/10.1175/1520-0485(1998)028<0634:GSABIO>2.0.CO;2

696 Halliwell, G. (2004). Evaluation of vertical coordinate and vertical mixing algorithms in the
697 hybrid-coordinate ocean model (HYCOM). *Ocean Modelling*, *7*(3–4), 285–322.
698 https://doi.org/10.1016/j.ocemod.2003.10.002
699 Hetland, R. D., Qu, L., & Hinson, K. E. (2025). Frontal Maintenance in Submesoscale Flows.
700 *Journal of Physical Oceanography*, *55*(2), 175–190. https://doi.org/10.1175/JPO-D-24-
701 0060.1
702 Hoskins, B. J. (1982). The Mathematical Theory of Frontogenesis. *Annual Review of Fluid*
703 *Mechanics*. Annual Reviews. https://doi.org/10.1146/annurev.fl.14.010182.001023
704 Hoskins, B., & Bretherton, F. (1972). Atmospheric frontogenesis models: Mathematical
705 formulation and solution. *Journal of the Atmospheric Sciences*, *29*, 11–37,
706 https://doi.org/10.1175/1520-0469(1972)029,0011: AFMMFA.2.0.CO;2.
707 Hoskins, B., James I., & White G. (1983). The shape, propagation and mean-flow interaction of
708 large-scale weather systems. *Journal of the Atmospheric Sciences*., *40*, 1595–1612.
709 https://doi.org/10.1175/1520-0469(1983)040<1595:TSPAMF>2.0.CO;2
710 Hu, J., Gan, J., Sun, Z., Zhu, J., & Dai, M. (2011). Observed three-dimensional structure of a
711 cold eddy in the southwestern South China Sea. *Journal of Geophysical Research*, *116*(C5),
712 C05016. https://doi.org/10.1029/2010JC006810
713 Jing, Z., Fox-Kemper, B., Cao, H., Zheng, R., & Du, Y. (2021). Submesoscale Fronts and Their
714 Dynamical Processes Associated with Symmetric Instability in the Northwest Pacific
715 Subtropical Ocean. *Journal of Physical Oceanography*, *51*(1), 83–100.
716 https://doi.org/10.1175/JPO-D-20-0076.1
717 Johnson, L., & Fox-Kemper, B. (2024). Modification of boundary layer turbulence by
718 submesoscale flows. *Flow*, *4*, E20. https://doi.org/10.1017/flo.2024.17

719 Kang, D., & Curchitser, E. N. (2015). Energetics of Eddy–Mean Flow Interactions in the Gulf
720 Stream Region. *Journal of Physical Oceanography*, *45*(4), 1103–1120.
721 https://doi.org/10.1175/JPO-D-14-0200.1
722 Klein, P., & Lapeyre, G. (2009). The Oceanic Vertical Pump Induced by Mesoscale and
723 Submesoscale Turbulence. *Annual Review of Marine Science*, *1*(1), 351–375.
724 https://doi.org/10.1146/annurev.marine.010908.163704
725 Lapeyre, G., and P. Klein (2006). Impact of the small scale elongated filaments on the oceanic
726 vertical pump, *Journal of Marine Research*, *64*, 835–851.
727 doi:10.1357/002224006779698369.
728 Lapeyre, G., Klein, P., & Hua, B. L. (2006). Oceanic Restratification Forced by Surface
729 Frontogenesis. *Journal of Physical Oceanography*, *36*(8), 1577–1590.
730 https://doi.org/10.1175/JPO2923.1
731 Lemarié, F., Kurian, J., Shchepetkin, A. F., Jeroen Molemaker, M., Colas, F., & McWilliams, J.
732 C. (2012). Are there inescapable issues prohibiting the use of terrain-following coordinates
733 in climate models? *Ocean Modelling*, *42*, 57–79.
734 https://doi.org/10.1016/j.ocemod.2011.11.007
735 Lévy, M., Ferrari, R., Franks, P. J. S., Martin, A. P., & Rivière, P. (2012). Bringing physics to
736 life at the submesoscale. *Geophysical Research Letters*, *39*, L14602.
737 https://doi.org/10.1029/2012GL052756
738 Li, Y., Han, W., Wilkin, J. L., Zhang, W. G., Arango, H., Zavala-Garay, J., et al. (2014).
739 Interannual variability of the surface summertime eastward jet in the South China Sea.
740 *Journal of Geophysical Research: Oceans*, *119*(10), 7205–7228.
741 https://doi.org/10.1002/2014JC010206

742 Lin, H., Liu, Z., Hu, J., Menemenlis, D., & Huang, Y. (2020). Characterizing meso- to
743 submesoscale features in the South China Sea. *Progress in Oceanography*, *188*, 102420.
744 https://doi.org/10.1016/j.pocean.2020.102420
745 Mahadevan, A. (2016). The Impact of Submesoscale Physics on Primary Productivity of
746 Plankton. *Annual Review of Marine Science*, *8*(1), 161–184.
747 https://doi.org/10.1146/annurev-marine-010814-015912
748 Mahadevan, A., & Tandon, A. (2006). An analysis of mechanisms for submesoscale vertical
749 motion at ocean fronts. *Ocean Modelling*, *14*(3–4), 241–256.
750 https://doi.org/10.1016/j.ocemod.2006.05.006
751 Marchesiello, P., Capet, X., Menkes, C., & Kennan, S. C. (2011). Submesoscale dynamics in
752 tropical instability waves. *Ocean Modelling*, *39*(1–2), 31–46.
753 https://doi.org/10.1016/j.ocemod.2011.04.011
754 Marshall, D. P., Maddison, J. R., & Berloff, P. S. (2012). A Framework for Parameterizing Eddy
755 Potential Vorticity Fluxes. *Journal of Physical Oceanography*, *42*(4), 539–557.
756 https://doi.org/10.1175/JPO-D-11-048.1
757 Martin, A. P., & Richards, K. J. (2001). Mechanisms for vertical nutrient transport within a
758 North Atlantic mesoscale eddy. *Deep Sea Research Part II: Topical Studies in*
759 *Oceanography*, *48*(4–5), 757–773. https://doi.org/10.1016/S0967-0645(00)00096-5
760 The MathWorksInc. (2022). MATLAB version: 9.13.0 (R2022b) [Software]. The MathWorks
761 Inc. https://www.mathworks.com
762 McKie, T., Lucas, A. J., & MacKinnon, J. (2024). Submesoscale Dynamics in the Bay of
763 Bengal: Inversions and Instabilities. *Journal of Geophysical Research: Oceans*. *129*(3).
764 https://doi.org/10.1029/2023JC020563

765 McWilliams, J. C. (2016). Submesoscale currents in the ocean. Proceedings of the Royal Society
766 A: Mathematical, *Physical and Engineering Sciences*, *472*(2189), 20160117.
767 https://doi.org/10.1098/rspa.2016.0117
768 McWilliams, J. C. (2017). Submesoscale surface fronts and filaments: Secondary circulation,
769 buoyancy flux, and frontogenesis. *Journal of Fluid Mechanics*, *823*, 391–432.
770 https://doi.org/10.1017/jfm.2017.294
771 McWilliams, J. C., Gula, J., Molemaker, M. J., Renault, L., & Shchepetkin, A. F. (2015).
772 Filament Frontogenesis by Boundary Layer Turbulence. *Journal of Physical*
773 *Oceanography*, *45*(8), 1988–2005. https://doi.org/10.1175/JPO-D-14-0211.1
774 McWilliams, J. C., Molemaker, M. J., & Olafsdottir, E. I. (2009). Linear Fluctuation Growth
775 during Frontogenesis. *Journal of Physical Oceanography*, *39*(12), 3111–3129.
776 https://doi.org/10.1175/2009JPO4186.1
777 McWilliams, J. C., Molemaker, M. J., & Yavneh, I. (2004). Ageostrophic, anticyclonic
778 instability of a geostrophic, barotropic boundary current. *Physics of Fluids*, *16*(10), 3720–
779 3725. https://doi.org/10.1063/1.1785132
780 Molemaker, M. J., Mcwilliams, J. C., & Capet, X. (2010). Balanced and unbalanced routes to
781 dissipation in an equilibrated Eady flow. *Journal of Fluid Mechanics*, *654*, 35–63.
782 https://doi.org/10.1017/S0022112009993272
783 Naveira Garabato, A. C., Yu, X., Callies, J., Barkan, R., Polzin, K. L., Frajka-Williams, E. E.,
784 et al. (2022). Kinetic energy transfers between mesoscale and submesoscale motions in the
785 open ocean's upper layers. *Journal of Physical Oceanography*, *52*(1), 75–97. https://doi.
786 org/10.1175/jpo-d-21-0099.1

O'Reilly, J.E., Maritorena, S., Mitchell, G., Siegel, D., Carder, K., Garver, S., et al. (1998). Ocean color chlorophyll algorithms for SeaWiFS. *Journal of Geophysical Research. 103,* 24937–24953. https://doi.org/10.1029/98JC02160

Pedlosky J. (1987). *Geophysical Fluid Dynamics* (pp. 499-503). New York, DC: Springer-Verlag.

Penven, P., Debreu, L., Marchesiello, P., & McWilliams, J. C. (2006). Evaluation and application of the ROMS 1-way embedding procedure to the central california upwelling system. *Ocean Modelling*, *12*(1–2), 157–187. https://doi.org/10.1016/j.ocemod.2005.05.002

Pham, H. T., & Sarkar, S. (2019). The role of turbulence in strong submesoscale fronts of the Bay of Bengal. *Deep Sea Research Part II: Topical Studies in Oceanography*, *168*, 104644. https://doi.org/10.1016/j.dsr2.2019.104644

Pietri, A., Capet, X., d'Ovidio, F., Levy, M., Le Sommer, J., Molines, J.-M., & Giordani, H. (2021). Skills and Limitations of the Adiabatic Omega Equation: How Effective Is It to Retrieve Oceanic Vertical Circulation at Mesoscale and Submesoscale? *Journal of Physical Oceanography*, *51*(3), 931–954. https://doi.org/10.1175/JPO-D-20-0052.1

Polzin, K. L. (2010). Mesoscale Eddy–Internal Wave Coupling. Part II: Energetics and Results from PolyMode. *Journal of Physical Oceanography*, *40*(4), 789–801. https://doi.org/10.1175/2009JPO4039.1

Qiao, J., Qiu, C., Wang, D., Huang, Y., & Zhang, X. (2023). Multi-Stage Development Within Anisotropy Insight of an Anticyclone Eddy in Northwestern South China Sea in 2021. *Geophysical Research Letters*, *50*(19), e2023GL104736. https://doi.org/10.1029/2023GL104736

809 Qiu, B., Chen, S., Klein, P., Wang, J., Torres, H., Fu, L.-L., & Menemenlis, D. (2018).
810 Seasonality in Transition Scale from Balanced to Unbalanced Motions in the World Ocean.
811 *Journal of Physical Oceanography*, *48*(3), 591–605. https://doi.org/10.1175/JPO-D-17-
812 0169.1
813 Qiu, C., He, B., Wang, D., Zou, Z., & Tang, H. (2023). Mechanisms of a shelf submesoscale
814 front in the northern South China Sea. *Deep Sea Research Part I: Oceanographic Research*
815 *Papers*, *202*, 104197. https://doi.org/10.1016/j.dsr.2023.104197
816 Qiu, C., Mao, H., Liu, H., Xie, Q., Yu, J., Su, D., et al. (2019). Deformation of a Warm Eddy in
817 the Northern South China Sea. *Journal of Geophysical Research: Oceans*, *124*(8), 5551–
818 5564. https://doi.org/10.1029/2019JC015288
819 Qiu, C., Yang, Z., Feng, M., Yang, J., Rippeth, T. P., Shang, X., et al. (2024). Observational
820 energy transfers of a spiral cold filament within an anticyclonic eddy. *Progress in*
821 *Oceanography*, *220*, 103187. https://doi.org/10.1016/j.pocean.2023.103187
822 Schubert, R., Gula, J., Greatbatch, R. J., Baschek, B., & Biastoch, A. (2020). The Submesoscale
823 Kinetic Energy Cascade: Mesoscale Absorption of Submesoscale Mixed Layer Eddies and
824 Frontal Downscale Fluxes. *Journal of Physical Oceanography*, *50*(9), 2573–2589.
825 https://doi.org/10.1175/JPO-D-19-0311.1
826 Scott, R. B., Arbic, B. K., Holland, C. L., Sen, A., & Qiu, B. (2008). Zonal versus meridional
827 velocity variance in satellite observations and realistic and idealized ocean circulation
828 models. *Ocean Modelling*, *23*(3–4), 102–112. https://doi.org/10.1016/j.ocemod.2008.04.009
829 Senior, N. V., Zhai, X., & Stevens, D. P. (2024). Zonal jets and eddy tilts in barotropic
830 geostrophic turbulence. *Journal of Fluid Mechanics*, *986*, A38.
831 https://doi.org/10.1017/jfm.2024.283

Shchepetkin, A. F., & McWilliams, J. C. (2005). The regional oceanic modeling system (ROMS): a split-explicit, free-surface, topography-following-coordinate oceanic model. *Ocean Modelling*, *9*(4), 347–404. https://doi.org/10.1016/j.ocemod.2004.08.002

Shearman, R. K., Barth, J. A., & Kosro, P. M. (1999). Diagnosis of the Three-Dimensional Circulation Associated with Mesoscale Motion in the California Current. *Journal of Physical Oceanography*, *29*, 651-670.https://doi.org/10.1175/1520-0485(1999)029<0651:DOTTDC>2.0.CO;2

Siegelman, L. (2020). Energetic Submesoscale Dynamics in the Ocean Interior. *Journal of Physical Oceanography*, *50*(3), 727–749. https://doi.org/10.1175/JPO-D-19-0253.1

Soci, C., Hersbach, H., Simmons, A., Poli, P., Bell, B., Berrisford, P., et al. (2024). The ERA5 global reanalysis from 1940 to 2022. *Quarterly Journal of the Royal Meteorological Society*. https://doi.org/10.1002/qj.4803

Srinivasan, K., Barkan, R., & McWilliams, J. C. (2023). A Forward Energy Flux at Submesoscales Driven by Frontogenesis. *Journal of Physical Oceanography*, *53*(1), 287–305. https://doi.org/10.1175/JPO-D-22-0001.1

Srinivasan, K., McWilliams, J. C., Renault, L., Hristova, H. G., Molemaker, J., & Kessler, W. S. (2017). Topographic and Mixed Layer Submesoscale Currents in the Near-Surface Southwestern Tropical Pacific. *Journal of Physical Oceanography*, *47*(6), 1221–1242. https://doi.org/10.1175/JPO-D-16-0216.1

Stewart, K. D., Spence, P., Waterman, S., Sommer, J. L., Molines, J.-M., Lilly, J. M., & England, M. H. (2015). Anisotropy of eddy variability in the global ocean. *Ocean Modelling*, *95*, 53–65. https://doi.org/10.1016/j.ocemod.2015.09.005

Sullivan, P. P., & McWilliams, J. C. (2018). Frontogenesis and frontal arrest of a dense filament in the oceanic surface boundary layer. *Journal of Fluid Mechanics*, *837*, 341–380. https://doi.org/10.1017/jfm.2017.833

Sullivan, P. P., & McWilliams, J. C. (2024). Oceanic Frontal Turbulence. *Journal of Physical Oceanography*, *54*(2), 333–358. https://doi.org/10.1175/JPO-D-23-0033.1

Tamarin, T., Maddison, J. R., Heifetz, E., & Marshall, D. P. (2016). A Geometric Interpretation of Eddy Reynolds Stresses in Barotropic Ocean Jets. *Journal of Physical Oceanography*, *46*(8), 2285–2307. https://doi.org/10.1175/JPO-D-15-0139.1

Taylor, J. R., & Ferrari, R. (2010). Buoyancy and wind-driven convection at mixed layer density fronts. *Journal of Physical Oceanography*, *40*(6), 1222–1242. https://doi.org/10.1175/2010jpo4365.1

Taylor, J. R., & Thompson, A. F. (2023). Submesoscale Dynamics in the Upper Ocean. *Annual Review of Fluid Mechanics*, *55*(1), 103–127. https://doi.org/10.1146/annurev-fluid-031422-095147

Thomas, L. N., Tandon, A., & Mahadevan, A. (2008). Submesoscale processes and dynamics. In M. W. Hecht & H. Hasumi (Eds.), *Geophysical Monograph Series* (Vol. 177, pp. 17–38). Washington, D. C.: American Geophysical Union. https://doi.org/10.1029/177GM04

Thomas, L. N., & Taylor, J. R. (2010). Reduction of the usable wind-work on the general circulation by forced symmetric instability. *Geophysical Research Letters*, *37*(18), 2010GL044680. https://doi.org/10.1029/2010GL044680

Thomas, L. N., Taylor, J. R., D'Asaro, E. A., Lee, C. M., Klymak, J. M., & Shcherbina, A. (2016). Symmetric Instability, Inertial Oscillations, and Turbulence at the Gulf Stream

876 Front. *Journal of Physical Oceanography*, *46*(1), 197–217. https://doi.org/10.1175/JPO-D-
877 15-0008.1
878 Thomas, L. N., Taylor, J. R., Ferrari, R., & Joyce, T. M. (2013). Symmetric instability in the
879 Gulf Stream. *Deep Sea Research Part II: Topical Studies in Oceanography*, *91*, 96–110.
880 https://doi.org/10.1016/j.dsr2.2013.02.025
881 Wang, Q., Dong, C., Dong, J., Zhang, H., & Yang, J. (2022). Submesoscale processes-induced
882 vertical heat transport modulated by oceanic mesoscale eddies. *Deep Sea Research Part II:*
883 *Topical Studies in Oceanography*, *202*, 105138. https://doi.org/10.1016/j.dsr2.2022.105138
884 Waterman, S., Hogg, N. G., & Jayne, S. R. (2011). Eddy–Mean Flow Interaction in the Kuroshio
885 Extension Region. *Journal of Physical Oceanography*, *41*(6), 1182–1208.
886 https://doi.org/10.1175/2010JPO4564.1
887 Waterman, S., & Hoskins, B. J. (2013). Eddy Shape, Orientation, Propagation, and Mean Flow
888 Feedback in Western Boundary Current Jets. *Journal of Physical Oceanography*, *43*(8),
889 1666–1690. https://doi.org/10.1175/JPO-D-12-0152.1
890 Waterman, S., & Jayne, S. R. (2011). Eddy-Mean Flow Interactions in the Along-Stream
891 Development of a Western Boundary Current Jet: An Idealized Model Study. *Journal of*
892 *Physical Oceanography*, *41*(4), 682–707. https://doi.org/10.1175/2010JPO4477.1
893 Waterman, S., & Lilly, J. M. (2015). Geometric Decomposition of Eddy Feedbacks in Barotropic
894 Systems. *Journal of Physical Oceanography*, *45*(4), 1009–1024.
895 https://doi.org/10.1175/JPO-D-14-0177.1
896 Wenegrat, J. O. (2023). The Current Feedback on Stress Modifies the Ekman Buoyancy Flux at
897 Fronts. *Journal of Physical Oceanography*, *53*(12), 2737–2749.
898 https://doi.org/10.1175/JPO-D-23-0005.1

899 Wenegrat, J. O., & Arthur, R. S. (2018). Response of the Atmospheric Boundary Layer to
900 Submesoscale Sea Surface Temperature Fronts. *Geophysical Research Letters*, *45*(24).
901 https://doi.org/10.1029/2018GL081034
902 Wenegrat, J. O., Thomas, L. N., Sundermeyer, M. A., Taylor, J. R., D'Asaro, E. A., Klymak, J.
903 M., et al. (2020). Enhanced mixing across the gyre boundary at the Gulf Stream front.
904 *Proceedings of the National Academy of Sciences*, *117*(30), 17607–17614.
905 https://doi.org/10.1073/pnas.2005558117
906 Xie, L., Liu, X., & Pietrafesa, L. J. (2007). Effect of Bathymetric Curvature on Gulf Stream
907 Instability in the Vicinity of the Charleston Bump. *Journal of Physical Oceanography*,
908 *37*(3), 452–475. https://doi.org/10.1175/JPO2995.1
909 Xue, H., & Bane, J. M. (1997). A Numerical Investigation of the Gulf Stream and Its Meanders
910 in Response to Cold Air Outbreaks. *Journal of Physical Oceanography*, *27*(12), 2606–2629.
911 https://doi.org/10.1175/1520-0485(1997)027<2606:ANIOTG>2.0.CO;2
912 Yang, J., Wang, D., Qiu, C., Zhai, X., Chen, R., Qiao, J., & Hong, B. (2025). Importance of
913 Strains in Kinetic Energy Flux for Submesoscale Processes from an Anisotropic Perspective
914 [Data set]. Zenodo. https://doi.org/10.5281/zenodo.17003445
915 Yu, X., Naveira Garabato, A. C., Martin, A. P., Buckingham, C. E., Brannigan, L., & Su, Z.
916 (2019a). An Annual Cycle of Submesoscale Vertical Flow and Restratification in the Upper
917 Ocean. *Journal of Physical Oceanography*, *49*(6), 1439–1461. https://doi.org/10.1175/JPO-
918 D-18-0253.1
919 Yu, X., Ponte, A. L., Elipot, S., Menemenlis, D., Zaron, E. D., & Abernathey, R. (2019b).
920 Surface Kinetic Energy Distributions in the Global Oceans From a High-Resolution

921 Numerical Model and Surface Drifter Observations. *Geophysical Research Letters*, *46*(16),
922 9757–9766. https://doi.org/10.1029/2019GL083074
923 Zeng, Q. (1982). Zonal Flow in Rotating Barotropic Atmosphere. *Journal of the Meteorological*
924 *Society of Japan*, *60*(1).
925 Zhai, X., & Marshall, D. P. (2013). Vertical Eddy Energy Fluxes in the North Atlantic
926 Subtropical and Subpolar Gyres. *Journal of Physical Oceanography*, *43*(1), 95–103.
927 https://doi.org/10.1175/JPO-D-12-021.1
928 Zhang, J., Zhang, Z., & Qiu, B. (2023). Parameterizing Submesoscale Vertical Buoyancy Flux
929 by Simultaneously Considering Baroclinic Instability and Strain-Induced Frontogenesis.
930 *Geophysical Research Letters*, *50*(8), e2022GL102292.
931 https://doi.org/10.1029/2022GL102292
932 Zhang, Z. (2024). Submesoscale Dynamic Processes in the South China Sea. *Ocean-Land-*
933 *Atmosphere Research*, *3*, 0045. https://doi.org/10.34133/olar.0045
934 Zhang, Z., Liu, Y., Qiu, B., Luo, Y., Cai, W., Yuan, Q., et al. (2023). Submesoscale inverse
935 energy cascade enhances Southern Ocean eddy heat transport. *Nature Communications*,
936 *14*(1), 1335. https://doi.org/10.1038/s41467-023-36991-2
937 Zhang, Z., Qiu, B., Klein, P., & Travis, S. (2019). The influence of geostrophic strain on oceanic
938 ageostrophic motion and surface chlorophyll. *Nature Communications*, *10*(1), 2838.
939 https://doi.org/10.1038/s41467-019-10883-w
940 Zhang, Z., Zhang, X., Qiu, B., Zhao, W., Zhou, C., Huang, X., & Tian, J. (2021). Submesoscale
941 Currents in the Subtropical Upper Ocean Observed by Long-Term High-Resolution
942 Mooring Arrays. *Journal of Physical Oceanography*, *51*(1), 187–206.
943 https://doi.org/10.1175/JPO-D-20-0100.1